JGR Space Physics

RESEARCH ARTICLE
10.1029/2022JA031236

Understanding Nighttime Ionospheric Depletions Associated With Sudden Stratospheric Warmings in the American Sector

M. Jones Jr.[1], L. P. Goncharenko[2], S. E. McDonald[1], K. A. Zawdie[1], J. Tate[3], F. Gasperini[4], N. M. Pedatella[5], D. P. Drob[1], and J. P. McCormack[1,6]

[1]Space Science Division, U.S. Naval Research Laboratory, Washington, DC, USA, [2]MIT Haystack Observatory, Westford, MA, USA, [3]Computational Physics, Inc., Springfield, VA, USA, [4]Orion Space Solutions, Louisville, CO, USA, [5]National Center for Atmospheric Research, High Altitude Observatory, Boulder, CO, USA, [6]Now at Heliophysics Division, Science Mission Directorate, NASA Headquarters, Washington, DC, USA

Key Points:

- Nighttime F-region plasma depletions are a robust feature of the American sector during sudden stratospheric warmings at low solar activity
- Deep nighttime decreases in electron density during the 2010 and 2013 stratospheric warming (SSWs) largely result from tidally modified meridional winds in thermospher e-ionosphere-mesosphere-electrodynamics general circulation model
- Recent satellite measurements of nighttime electron density decreases and thermospheric winds during the 2021 SSW validate model results

Supporting Information:

Supporting Information may be found in the online version of this article.

Correspondence to:

M. Jones Jr,
mcarthur.jones@nrl.navy.mil

Citation:

Jones, M. Jr., Goncharenko, L. P., McDonald, S. E., Zawdie, K. A., Tate, J., Gasperini, F., et al. (2023). Understanding nighttime ionospheric depletions associated with sudden stratospheric warmings in the American sector. *Journal of Geophysical Research: Space Physics*, *128*, e2022JA031236. https://doi.org/10.1029/2022JA031236

Received 20 DEC 2022
Accepted 12 MAY 2023

Abstract This study focuses on understanding what drives the previously observed deep nighttime ionospheric hole in the American sector during the January 2013 sudden stratospheric warming (SSW). Performing a set of numerical experiments with the thermosphere-ionosphere-mesosphere-electrodynamics general circulation model (TIME-GCM) constrained by a high-altitude version of the Navy Global Environmental Model, we demonstrate that this nighttime ionospheric hole was the result of increased poleward and down magnetic field line plasma motion at low and midlatitudes in response to altered *F*-region neutral meridional winds. Thermospheric meridional wind modifications that produced this nighttime depletion resulted from the well-known enhancements in semidiurnal tidal amplitudes associated with stratospheric warming (SSWs) in the upper mesosphere and thermosphere. Investigations into other deep nighttime ionospheric depletions and their cause were also considered. Measurements of total electron content from Global Navigation Satellite System receivers and additional constrained TIME-GCM simulations showed that nighttime ionospheric depletions were also observed on several nights during the January-February 2010 SSW, which resulted from the same forcing mechanisms as those observed in January 2013. Lastly, the recent January 2021 SSW was examined using Modern-Era Retrospective Analysis for Research and Applications, Version 2, COSMIC-2 Global Ionospheric Specification electron density, and ICON Michelson Interferometer for Global High-Resolution Thermospheric Imaging horizontal wind data and revealed a deep nighttime ionospheric depletion in the American sector was likely driven by modified meridional winds in the thermosphere. The results shown herein highlight the importance of thermospheric winds in driving nighttime ionospheric variability over a wide latitude range.

1. Introduction

Understanding the mechanisms that drive ionospheric variability is paramount for forecasting space weather impacts on essential communication and space-based technologies. Short-term ionospheric variability can be forced from above via solar flares, coronal mass ejections and subsequent geomagnetic storms that drive energetic particle precipitation, high-speed solar wind streams, or even a solar eclipse. However, ionospheric variability can also be driven from below via lower atmospheric meteorology, and during times of weak solar activity, lower and middle atmospheric meteorological forcing is responsible for a considerable amount of the observed ionospheric variability. Recent reviews by Chau et al. (2012), H. L. Liu (2016), Baldwin et al. (2021), and L. P. Goncharenko et al. (2021) present the copious pathways through which lower atmospheric weather drives ionospheric variability, with perhaps no one meteorological phenomenon more reported on than a sudden stratospheric warming (SSW).

Sudden stratospheric warmings are large-scale meteorological events that occur in the winter hemisphere and are driven by the dissipation of tropospheric planetary waves at stratospheric altitudes. In the stratosphere, SSWs are characterized by prominent local increases in polar stratospheric temperatures and deceleration of high-latitude zonal winds around 10 hPa, but their effects are felt throughout the entire atmosphere (N. M. Pedatella et al., 2018). Stening (1977), and Stening et al. (1996) were the first to hypothesize that SSWs could drive ionospheric variability, which was later clearly demonstrated by a series of studies including L. Goncharenko and Zhang (2008), Chau et al. (2009), and L. P. Goncharenko, Chau, et al. (2010). Now it is widely established that SSWs have profound

effects on the ionosphere and its variability, which may even extend into the plasmasphere up to several Earth radii away, as suggested in a recent study by Jones Jr. et al. (2020).

Although the links between SSWs and ionospheric variability are well established, many prior research efforts have focused on understanding the longitudinal ionospheric variability associated with SSWs and/or daytime ionospheric changes related to SSWs at low and mid-latitudes (e.g., L. P. Goncharenko, Coster, et al., 2010; Maute et al., 2015; N. M. Pedatella & Maute, 2015; N. M. Pedatella et al., 2016; McDonald et al., 2018; N. Pedatella, 2022, and a number of others). This is largely due to the causal link between global-scale atmospheric solar tides, lunar tides, and planetary wave variability and ionospheric variability during SSWs (e.g., N. M. Pedatella & Liu, 2013; Siddiqui et al., 2021; Yamazaki et al., 2020; and many others). However, a comparatively smaller number of studies have focused on understanding and characterizing SSW-driven variability in the nighttime ionosphere. From ionosonde measurements, Sumod et al. (2012) reported that foF_2 (critical frequency of the F_2 layer of the ionosphere) was notably lower after sunset during the minor SSW of January 2008 at Trivandrum in the Indian longitude sector. Fagundes et al. (2015) also reported large foF_2 variations occurring in the evening/nighttime over South America during the major SSW of January 2009. Mošna et al. (2021) recently showed nighttime enhancements in the total electron content rate index over Europe during the SSWs of February 2018 and December-January 2018-2019 which they ascribe to both lower atmospheric and geomagnetic forcing.

As inferred from the previous studies summarized above, SSW-forced nighttime ionospheric changes (i.e., their magnitude and relative variations) vary with longitude. The most striking nighttime ionospheric variations associated with SSWs were reported by L. P. Goncharenko et al. (2018) (hereafter referred to as G18) during the major SSW of January 2013. Using Global Navigation Satellite System receivers, digisondes, and incoherent scatter radar observations at low and middle latitudes (~55°S to ~45°N) in the American sector, G18 reported on a deep depletion in total electron content (TEC) reaching a factor of 2–5 relative to background conditions between local midnight and local sunrise for four consecutive nights. G18 hypothesized a few different mechanisms that could be responsible for driving these observed depletions in the nighttime ionosphere, including atmospheric solar tidal and lunar tidal modifications in thermospheric winds at *F*-region altitudes associated with the January 2013 SSW. G18 suggested that while both zonal and meridional components of the neutral wind field could be contributing to the observed ionospheric nighttime depletions (e.g., Miyoshi et al., 2015), it was more likely driven by *F*-region zonal winds than meridional winds. They specifically cited that SSW driven changes in the zonal winds could strongly force ionospheric electron density changes due to magnetic declination, such as those described in S.-R. Zhang et al. (2012). However, G18 acknowledged that their zonal wind hypothesis needed additional experimental and modeling support.

This study therefore seeks to evaluate the hypothesis described by G18 for producing deep nighttime ionospheric depletions in the American sector during SSWs using a set of numerical experiments performed with a hierarchy of first-principles models. Specifically, we perform an initial set of numerical experiments with the NCAR thermosphere-ionosphere-mesosphere-electrodynamics general circulation model (TIME-GCM) constrained by meteorological analyses in the middle atmosphere from the high-altitude version of the Navy Global Environmental Model (NAVGEM-HA, McCormack et al., 2017; Eckermann et al., 2018), and evaluate the model's capability of reproducing the ionospheric observations reported by G18. Then, we further evaluate these constrained TIME-GCM simulations to diagnose the thermospheric zonal and meridional wind behavior at *F*-region altitudes during January 2013. To characterize the extent to which SSW-altered tidal activity drives thermospheric wind variations, additional NCAR thermosphere-ionosphere-electrodynamics general circulation model (TIE-GCM) simulations were performed in order to preferentially force different tidal components thought to be important in generating the observed deep ionospheric hole. We lastly evaluate if thermospheric wind forcing of an ionospheric hole in the American sector occurs during other SSW events, including the SSW of January-February 2010, as well as the more recent January 2021 SSW using both models and state-of-the-art upper atmospheric observations.

The combined data-model results presented herein illustrate that nighttime ionospheric depletions in the American sector occur in all of the SSWs investigated, and that these nighttime depletions are preferentially forced by SSW-altered *F*-region meridional winds acting to push plasma down magnetic field lines. We also show that the onset of these nighttime ionospheric depletions varies with each middle atmospheric disturbance, sometimes occurring several days to a week after the initial zonal wind reversal in the stratosphere, and other times aligning with the associated mesospheric cooling. Lastly, our numerical experiments highlight the important role

of semidiurnal migrating tidal (SW2, or the semidiurnal westward propagating tide with zonal wavenumber 2) enhancements associated with SSWs in driving *F*-region nighttime ionospheric depletions, which are quantified using a hierarchy of thermosphere-ionosphere (TI) models that allow the user to control different parts of the vertically propagating wave spectrum.

2. Observations, Models, and Simulations

This section provides a general overview of the ionospheric and thermospheric observations used, brief descriptions of the models employed, and an outline of the modeling simulations performed. Where possible, the reader is referred to the original study(ies) that describe each observation and model in detail, while summarizing how a specific data set or model was used as part of this work.

2.1. Ionospheric Observations

2.1.1. GNSS Data

Nighttime ionospheric depletions are identified in this study following the work of G18 using TEC derived from a global network of Global Navigation Satellite System (GNSS) receivers that are available beginning in 2000 (Rideout & Coster, 2006) from the CEDAR Madrigal website (http://cedar.openmadrigal.org/). This database includes ionospheric observations from a varying number of receivers, starting with ∼500 receivers in the year 2000 and increasing to ∼1,000 receivers by 2013. The American longitudinal sector is selected for this study, as it provides the best GNSS data coverage and allows investigations of ionospheric features as a function of latitude. Initial GNSS data are available with 5-min temporal resolution and 1° × 1° spatial resolution. We selected data at the −75° longitude (±7.5°) and organized it in 1-hr bins, preserving the 1° resolution in latitude. GNSS TEC are used to validate constrained TIME-GCM/NAVGEM-HA results for the January 2013 and January-February 2010 SSW events.

2.1.2. FORMOSAT-7/COSMIC-2 GIS

The FORMOSAT-7/COSMIC-2 (Formosa Satellite 7/Constellation Observing System for Meteorology, Ionosphere, and Climate 2) is a six satellite mission launched in June 2019 that reached its final configuration in February 2021, whereby the six satellites orbit at an altitude of near 530 km and are separated by ∼60° in longitude (C.-Y. Lin et al., 2020). Each satellite provides in situ electron density measurements from the Ion Velocity Meter (IVM), as well as several thousand electron density profiles per day obtained using radio occultation (RO).

The Global Ionospheric Specification (GIS) data assimilation product was developed by C. Y. Lin et al. (2015); C. Y. Lin et al. (2017) using a Gauss-Markov Kalman Filter and assimilates slant TEC from ground-based GNSS measurements and spaced-based FORMOSAT-7/COSMIC-2 RO measurements into the background International Reference Ionosphere 2016 (IRI2016, Bilitza et al., 2017), to provide hourly three-dimensional electron density on a 2.5° × 5° × 20 km grid (longitude × latitude × altitude), from pole-to-pole, and 120–700 km altitude. Recent work by J. T. Lin et al. (2020), C.-Y. Lin et al. (2020), Rajesh et al. (2021), and Oberheide (2022) all demonstrate the advantages and quality of the GIS data set for studying ionospheric variability. Specifically, Oberheide (2022) used the GIS data set to investigate daily variations in the semidiurnal tidal spectrum at *F*-region altitudes during the January 2021 SSW. In this study, we use GIS electron density at 260 km, which is close to the altitude of the peak nighttime electron density in the *F*-region, from December 2020-February 2021 in the American sector to highlight nighttime ionospheric depletions associated with the January 2021 SSW.

2.2. TEC Empirical Model

To isolate lower atmospheric (e.g., SSW) and other impacts on ionospheric variability from the well-known forcing from solar and geomagnetic activity, and seasonal variations, G18 created an empirical model of numerous ionospheric parameters, including TEC. The same TEC empirical model is used here. It is based on 15 years of GNSS observations spanning the winter season (1 November–31 March). Model inputs include geographic latitude, day of year, universal time, solar activity (F10.7 cm index), and geomagnetic activity (Ap3 index). Model coefficients are calculated using a least squares fit to available GNSS TEC data, and these model coefficients are determined every 1° in latitude in order to provide sufficient spatial resolution to capture tidal variations in latitude. For a more detailed description of the TEC empirical model used herein, the reader is referred to G18.

G18 demonstrated that TEC residuals and uncertainties could be used to isolate nighttime ionospheric anomalies associated with the January 2008, 2012, and 2013 SSWs. In the present study, we use this TEC empirical model to validate anomalously low nighttime TEC values in the American sector simulated by the TIME-GCM/NAVGEM-HA during the January-February 2010 and January 2013 SSWs.

2.3. Thermospheric Observations

2.3.1. ICON MIGHTI

The Ionospheric Connection Explorer (ICON, Immel et al., 2017) was launched in October 2019 to understand how the lower atmosphere is connected to the space environment via the ionosphere. ICON is in a ∼27° inclination orbit and provides observations between roughly 10°S to 40°N in latitude. One of the four instruments onboard ICON is the Michelson Interferometer for Global High-Resolution Thermospheric Imaging (MIGHTI, Englert et al., 2015; Englert et al., 2017) designed to measure horizontal thermospheric winds at low and middle latitudes between about 90 and 300 km. MIGHTI measures interferometric limb images of both green (557.7 nm) and red (630.0 nm) line emissions of atomic oxygen, resulting in wind measurements continuously between ∼90–300 km during daytime, and between ∼90 and ∼110 km (green line) and ∼210 and ∼300 km (red line) during nighttime.

In this study, we utilize the MIGHTI nighttime red line horizontal winds, data version v04, to understand changes in nighttime thermospheric winds at *F*-region altitudes during the January 2021 SSW event. MIGHTI nighttime red line horizontal winds at ∼240 km, data version v03, have been recently validated by Makela et al. (2021) using two ground-based Fabry-Perot interferometers, one of which is located in the American sector (Urbana, Illinois, −88.16° longitude, 40.17° latitude). Compared to the v03 product, v04 winds include an updated correction for long-term mechanical drift and precession cycle variation.

"Daily nighttime zonal mean" zonal and meridional winds in the American sector are obtained from ICON MIGHTI as the average of all nighttime (18–24 and 0–6 local time (LT)) data within −90° to −50° longitude during December 2020 through to January 2021. Zonal and meridional wind MIGHTI data reported on herein are 3-day running means (centered on the day of interest) and are averaged in 5° latitude bins. Minor effects from local time variations with latitude and changes in the longitudinal separation of sampling along each orbit are expected; however, due to the 3-day and latitudinal-longitudinal averaging used herein, these orbital and sampling characteristics are unlikely to notably impact our results. Also, some impacts from the MIGHTI local time precession can be expected, especially when sampling occurs near the solar terminators. Following Forbes et al. (2022) and Gasperini et al. (2022), to achieve the desired spatial-temporal coverage, wind quality data equal to 0 are excluded from the analysis, while data with quality flag equal to 0.5 are included. Many of the 0-flagged data are connected with South Atlantic Anomaly contamination, as well as data near the solar terminators. Their removal leaves gaps between −90° and −30° longitude in the Southern Hemisphere that are not significantly affecting the latitude regions of primary interest for this study.

2.4. Models and Simulations

2.4.1. MERRA2

The National Aeronautics and Space Administration (NASA) Modern-Era Retrospective Analysis for Research and Applications, Version 2 (MERRA2) is a lower and middle atmospheric reanalysis that extends from the surface to 0.01 hPa or ∼70–80 km (Gelaro et al., 2017). MERRA2 assimilates a full suite of both ground- and space-based meteorological observations, including satellite radiance observations that extend into the stratosphere (e.g., McCarty et al., 2016). Three-hourly (3-hr) MERRA2 output of horizontal winds and temperatures, and in some cases other important tropospheric, stratospheric, and mesospheric parameters are commonly used to constrain whole atmosphere and middle and upper atmospheric general circulation models in order to realistically drive TI variability due to lower atmospheric sources. For example, N. Pedatella (2022) used the specified dynamics (SDs) approach of Smith et al. (2017) to constrain the lower and middle atmospheric horizontal winds and temperatures of the National Center for Atmospheric Research (NCAR) Whole Atmosphere Community Climate Model with thermosphere-ionosphere eXtension (WACCM-X) using MERRA2 dynamical fields up to 50 km to reproduce the atmospheric conditions during the January 2021 SSW.

To describe the January 2021 SSW, we use 3-hr stratospheric and mesospheric zonal winds and temperatures on the native model grid with a horizontal grid spacing of 0.625° in longitude by 0.5° in latitude during the boreal winter months of 2020–2021. Previous studies, including Maute et al. (2015), Oberheide et al. (2020), Oberheide (2022), and many others have used MERRA2, and/or its predecessor MERRA (Rienecker et al., 2011) to describe the timing and severity of SSWs and concomitant observed TI variability.

2.4.2. NAVGEM-HA

NAVGEM-HA is a middle atmospheric extension of the US Navy's numerical weather prediction system (Hogan et al., 2014) developed for stratospheric and mesospheric research applications. The reader is referred to McCormack et al. (2017), Eckermann et al. (2018), and references therein for a detailed description of NAVGEM-HA. Middle atmospheric data assimilation of three additional satellite datasets are used to supplement the operational tropospheric and stratospheric observables used in the operational forecasts including (a) temperature, ozone mixing ratio, and water vapor mixing ratio (version 4) retrievals from the Microwave Limb Sounder (MLS) on board the NASA Aura satellite (Yan et al., 2016); (b) temperature profiles from version 2.0 SABER retrievals (Rezac et al., 2015); and (c) microwave radiances from the upper atmosphere sounding channels of the Special Sensor Microwave Imager/Sounder (SSMIS) on the Defense Meteorological Satellite Program (DMSP) platforms (Swadley et al., 2008). Global analyses of horizontal winds and temperatures are produced every 6 hr, which are then used to initialize short-term forecasts, leading to a daily 3 hr analysis/forecast product extending up to ∼100 km.

Independent validation of NAVGEM-HA wind fields against ground-based wind and temperature measurements was provided by McCormack et al. (2017), Eckermann et al. (2018), Jones Jr. et al. (2020), and Stober et al. (2020). Dhadly et al. (2018) independently validated NAVGEM-HA atmospheric tidal amplitudes and phases in the mesosphere and lower thermosphere (MLT) against the Thermosphere-Ionosphere-Mesosphere Energetics and Dynamics Doppler Interferometer (TIMED TIDI) wind measurements (Killeen et al., 1999, 2006; Niciejewski et al., 2006), while Eckermann et al. (2018) showed that NAVGEM-HA temperatures compared favorably with the Solar Occultation for Ice Experiment (SOFIE) instrument on the Aeronomy of Ice in the Mesosphere (AIM) explorer (Bailey et al., 2014). Also, Siskind et al. (2021) validated NAVGEM-HA tracers (e.g., H_2O) in the mesosphere against SOFIE observations. For this work, NAVGEM-HA horizontal wind and temperature fields are used to constrain the middle atmosphere of TIME-GCM in order to accurately reproduce the January-February 2010 and January 2013 SSWs.

2.4.3. NCAR Thermospheric General Circulation Models

The NCAR thermospheric general circulation models (TGCMs) are hydrostatic global general circulation models that self-consistently simulate the dynamics, chemistry, energetics, and electrodynamics of Earth's middle and upper atmosphere. These TGCMs solve the continuity, electrodynamic, energy, and momentum equations from first-principles on a spherical grid in longitude, latitude, and log-pressure coordinates extending up to $\sim 4.6 \times 10^{-10}$ hPa or roughly 500–700 km altitude, depending on solar cycle. The TGCMs consist of two models, an exclusive thermosphere-ionosphere model, or TIE-GCM whose lower boundary is at ∼97 km ($\sim 5.5 \times 10^{-4}$ hPa), and a model that includes the upper stratosphere and mesosphere, the TIME-GCM with a lower boundary of ∼12 hPa or (∼30 km). We use both TGCMs in this study. For more details on the historical development of the TGCMs the reader is referred to Dickinson et al. (1984), Richmond et al. (1992), Roble and Ridley (1994), Roble (1996), Qian et al. (2014), and references therein, while Jones Jr. et al. (2020) provides a more detailed description on some of the model physics differences between TIME- and TIE-GCM.

All TGCM simulations performed as part of this study (i.e., TIME- and TIE-GCM simulations) were done using a model resolution of 2.5° × 2.5° (longitude x latitude) with four model grid points per vertical scale height. Further, all TGCM simulations were run using measured space weather conditions, including daily and 81-day averaged values of the F10.7 cm solar radio flux and 3-hourly Kp. Solar irradiance values spanning the X-ray and extreme ultraviolet (EUV) regions of the solar spectrum follow the formulation presented by Solomon and Qian (2005), while far ultraviolet solar radiation is specified by Woods and Rottman (2002). Temporal variations in X-rays, EUV, and FUV radiation are then accounted for by scaling the Richards et al. (1994) EUVAC model using the measured F10.7. High latitude forcing is parameterized using an empirical ion convection model by Heelis et al. (1982) and a default analytical auroral particle precipitation model by Roble and Ridley (1987), the strength of which is determined using the 3-hourly Kp values (after Emery et al., 2012).

2.4.4. TIME-GCM Simulations

To investigate the processes responsible for driving the observed nighttime ionospheric variability in the American sector reported by G18 several TIME-GCM simulations were performed for the January-February 2010 and January 2013 SSWs. In most cases, the TIME-GCM cannot self-consistently reproduce a SSW without being constrained by realistic stratospheric and mesospheric winds and temperatures. Therefore, to simulate the January-February 2010 and January 2013 SSWs, we conducted TIME-GCM simulations in which middle atmospheric horizontal winds and temperatures between the model lower boundary (~30 km) and ~97 km were constrained using NAVGEM-HA using four-dimensional tendency nudging (originally called 4D data assimilation by Stauffer and Seaman (1990) and Stauffer and Seaman (1994)). This nudging technique is described in great detail by Jones Jr. et al. (2018), and consists of adding an additional momentum or energy tendency term to the conservation equations that is proportional to the modeled and NAVGEM-HA horizontal wind and temperature differences up to ~97 km. The model is unconstrained above ~97 km (i.e., log-pressure level −7).

Constrained TIME-GCM/NAVGEM-HA simulations for the January 2013 SSW are identical to those reported by Jones Jr. et al. (2020), using realistic time-varying solar and geomagnetic inputs. Constrained simulations for January-February 2010 are almost identical to those performed by Jones Jr. et al. (2018), except with one important caveat; TIME-GCM eddy diffusion coefficient values (k_{zz}) were not reduced by a factor of 10 in this study. While this change leads to a reduction in the absolute atomic oxygen concentration (and therefore electron density) in the thermosphere due to increased vertical transport driven by including realistic wave perturbations, it has minimal impact on the ionospheric variations reported on herein (e.g., Jones Jr. et al., 2018; Siskind et al., 2014; Siskind et al., 2019), and therefore does not impact our conclusions. Note that TIME-GCM simulations constrained by NAVGEM-HA are subsequently referred to as "Nudged" simulations.

To quantify how "deep" the simulated TIME-GCM/NAVGEM-HA nighttime ionospheric hole is relative to climatology, additional baseline TIME-GCM simulations were performed for the boreal winters of 2009–2010 and 2012–2013. "Baseline" TIME-GCM simulations are not constrained, but driven at the model lower boundary by climatological zonal and diurnal mean winds, temperatures, and geopotential heights, and diurnal and semidiurnal migrating and non-migrating tides from the Global Scale Wave Model 2009 (GSWM-09, X. Zhang et al., 2010a, 2010b). Additional TIME-GCM simulations were performed to isolate the role of specific forcing terms in the O^+ continuity equation. These will be discussed in more detail in Section 3.1.

2.4.5. TIE-GCM Simulations

The spectrum of waves that enters the upper atmosphere can be quite different during SSWs (e.g., Lieberman et al., 2022; G. Liu et al., 2022; Oberheide, 2022; Yiğit & Medvedev, 2016; and many others). G18 suggested that nighttime electron density variations during SSWs could be driven by thermospheric horizontal wind perturbations in the *F*-region due to upward propagating semidiurnal tides. Specifically, SW2 is preferentially enhanced during SSWs (Siddiqui et al., 2019) and known to drive TI variability during SSWs (e.g., N. M. Pedatella et al., 2014), but is mainly forced by ozone absorption of UV in the upper stratosphere, and is internally generated in the TIME-GCM. Thus, in order to quantify the impact of SW2 on modeled nighttime ionospheric depletions associated with SSWs, we employ the TIE-GCM whose model lower boundary is at the mesopause, well above the lower and middle atmospheric source region of SW2.

Similar to simulations performed by N. M. Pedatella (2016), we performed TIE-GCM simulations whose lower boundary is forced by constrained TIME-GCM/NAVGEM-HA output during the January 2013 and January-February 2010 SSWs. Again, TIE-GCM simulations for the January 2013 SSW are identical to those reported by Jones Jr. et al. (2020). TIE-GCM simulations for the January-February 2010 SSW are performed in the same way as the January 2013 SSW, that is lower boundary horizontal winds, neutral temperatures, and geopotential heights were specified using hourly horizontal wind, neutral temperature, and geopotential height outputs at model log-pressure level −7 from TIME-GCM/NAVGEM-HA simulations. For the different time periods, differences between simulations with and without SW2 at the model lower boundary elucidate the role of SW2 in driving nighttime ionospheric depletions in the American sector. Note simulations that include SW2 (and all other wave perturbations at the TIE-GCM lower boundary) are subsequently referred to as "All Waves," while simulations excluding SW2 forcing at the lower boundary are referred to as "w/o SW2."

Additional "Baseline" TIE-GCM simulations were also performed to further provide climatological context to SSW-driven SW2 effects on nighttime ionospheric depletions. In these baseline TIE-GCM simulations,

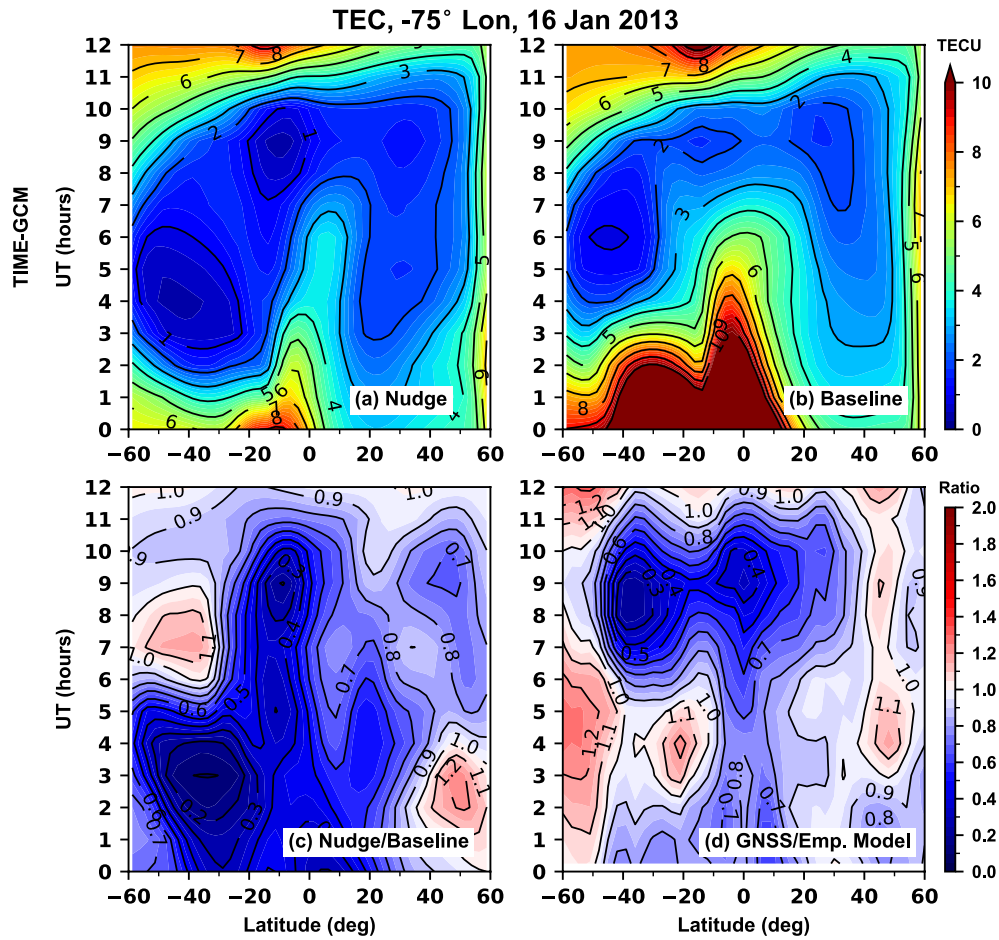

Figure 1. Total electron content (TEC) from −75° longitude on 16 January 2013 as a function of latitude and universal time. Shown are TEC values from thermosphere-ionosphere-mesosphere-electrodynamics general circulation high-altitude version of the Navy Global Environmental Model (TIME-GCM/NAVGEM-HA).Nudge (a), TIME-GCM Baseline (b), TIME-GCM Nudge to Baseline TEC ratio (c), the data to empirical model ratio from GNSS TEC (d). Note 0–12 UT corresponds to 19-7 LT at −75° longitude.

background (or zonal and diurnal averaged) wind, temperature, and geopotential height fields at the model lower boundary were specified by latitude- and month-dependent mean winds calculated from combined Wind Imaging Interferometer (WINDII)—High-Resolution Doppler Imager (HRDI) measurements (see Forbes et al., 2002), and mean temperatures and geopotential heights from Sounding of the Atmosphere using Broadband Emission Radiometry (SABER) measurements (see X. Zhang et al., 2010a, 2010b). Migrating and non-migrating diurnal and semidiurnal tidal perturbations (with zonal wave numbers between ±6) generated in the troposphere, stratosphere, and mesosphere from the Climatological Tidal Model of the Thermosphere (CTMT, see Oberheide et al., 2011) are also included at the model lower boundary. For more details on the "Baseline" TIE-GCM configuration and the climatological observationally based lower boundary conditions the reader is referred to Jones et al. (2014) and Jones Jr. et al. (2019).

3. Results and Discussion

3.1. January 2013 SSW

First, we briefly describe the stratospheric, mesospheric, and space weather conditions during the January 2013 SSW. L. Goncharenko, Hsu, et al. (2013) (Figure 1), Maute et al. (2015) (Figures 1–3), N. M. Pedatella and Maute (2015) (Figure 6), and Jones Jr. et al. (2020) (Figure 2 and Figure S2 in Supporting Information S1) all illustrate the middle atmospheric dynamic and thermodynamic conditions, as well as the solar and geomagnetic

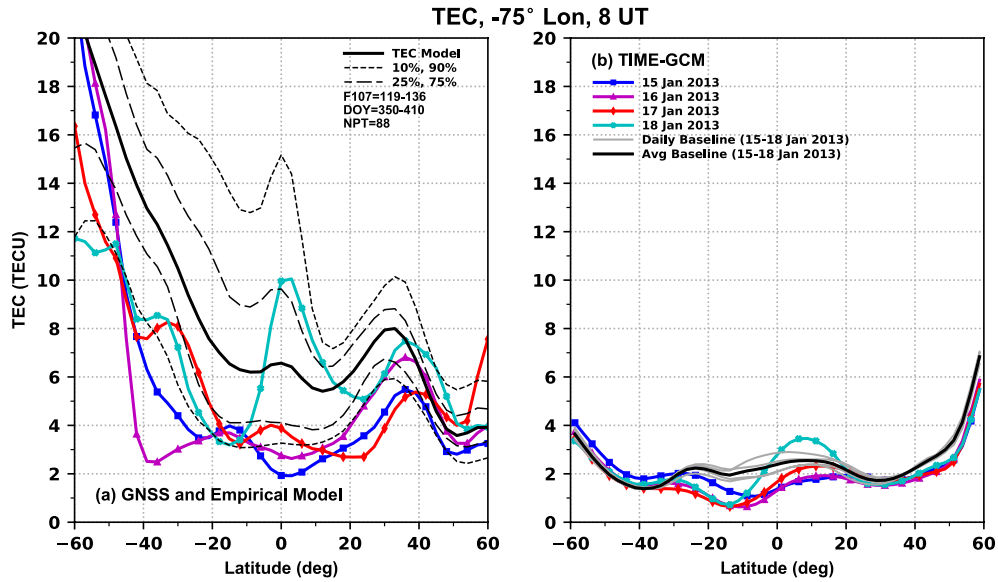

Figure 2. Latitudinal variations of total electron content (TEC) at −75° longitude and 8 UT (3 LT) as measured by Global Navigation Satellite System (GNSS), predicted by the GNSS empirical model (a), and simulated by the thermospher e-ionosphere-mesosphere-electrodynamics general circulation (TIME-GCM) (b). Panel (a) is an adaption of Figure 4 from G18, where the GNSS TEC observations for four different nights are shown in the colored lines and predicted TEC values from the empirical models are shown in black lines. Thick dash lines show 25th and 75th percentiles of all TEC values observed within 7.5° from −75°, for a range of F10.7 = 119–135 and from mid-December to mid-February. Thin dash lines show 10th and 90th percentiles, respectively. The colored TEC latitudinal profiles in panel (b) are from the Nudged TIME-GCM simulation, gray lines indicate TEC latitudinal profiles from the Baseline TIME-GCM simulation, and the thick black line is the average TEC from 15 to 18 January 2013 Baseline TIME-GCM simulation.

situation during the January 2013 SSW for the interested reader. A long duration (i.e., 3–4 weeks) major (as defined by Butler et al. (2015)) SSW began on 6 January 2013, when zonal mean temperatures in the northern high latitude stratosphere increased by 20–30 K, while overlying zonal mean mesospheric temperatures decreased by the same amount, and zonal mean stratospheric winds at 60°N and 10 hPa reversed from eastward to westward. Zonal mean zonal winds at 60°N and 10 hPa remained westward until 27 and 28 January and an associated elevated stratopause (~80 km) developed at roughly the same time (e.g., Limpasuvan et al., 2016; Manney et al., 2009; Siskind et al., 2010), marking the so-called "extended" recovery phase in the middle atmosphere. This SSW was coincident with a notable change in F10.7 due to the 27-day solar rotation period, with daily F10.7 values increasing from roughly 110 sfu in mid-December 2012 to ~168 sfu on 10 January, which then subsequently subsided to daily values of ~100–110 sfu by 18 January. Also, geomagnetic activity in January 2013, while weak (i.e., Kp ≤ 4), was slightly elevated relative to December 2012 and February 2013. Previous work by Maute et al. (2015) indicated that this slightly elevated geomagnetic activity contributed to the SSW response in equatorial plasma drifts in the American-African sector. Even with the elevated solar and geomagnetic drivers and associated impacts, daytime ionospheric anomalies reported by L. Goncharenko, Hsu, et al. (2013) and Jonah et al. (2014) were quite large and persisted ~3–6 weeks, while G18 demonstrated a clear nighttime depletion between 14 and 18 January 2013 associated with this SSW.

Figures 1a and 1b show TEC from the Nudge and Baseline TIME-GCM simulations, respectively, on 16 January 2013 at −75° longitude as a function of latitude and 0–12 UT (19-7 LT). Overall TEC values in the nudged simulation are smaller compared to the baseline simulation, especially at latitudes southward of 20° N between 0 and 4 UT, and southern equatorial latitudes throughout most of the night. To more directly compare with the results of G18, Figure 1c depicts the modeled TEC anomaly from TIME-GCM expressed as a nudged-to-baseline ratio, $TEC_{Nudge}/TEC_{Baseline}$. Figure 1c better highlights the nighttime TEC depletions already discussed, but also demonstrates the degree to which nighttime ionospheric electron densities in the American sector were depressed following the January 2013 SSW.

Figure 1d is a reproduction of Figure 5 in G18 and illustrates the data-to-empirical model ratio for GNSS TEC at the same date, location, and time as our TIME-GCM results. In general, the TEC anomalies simulated by

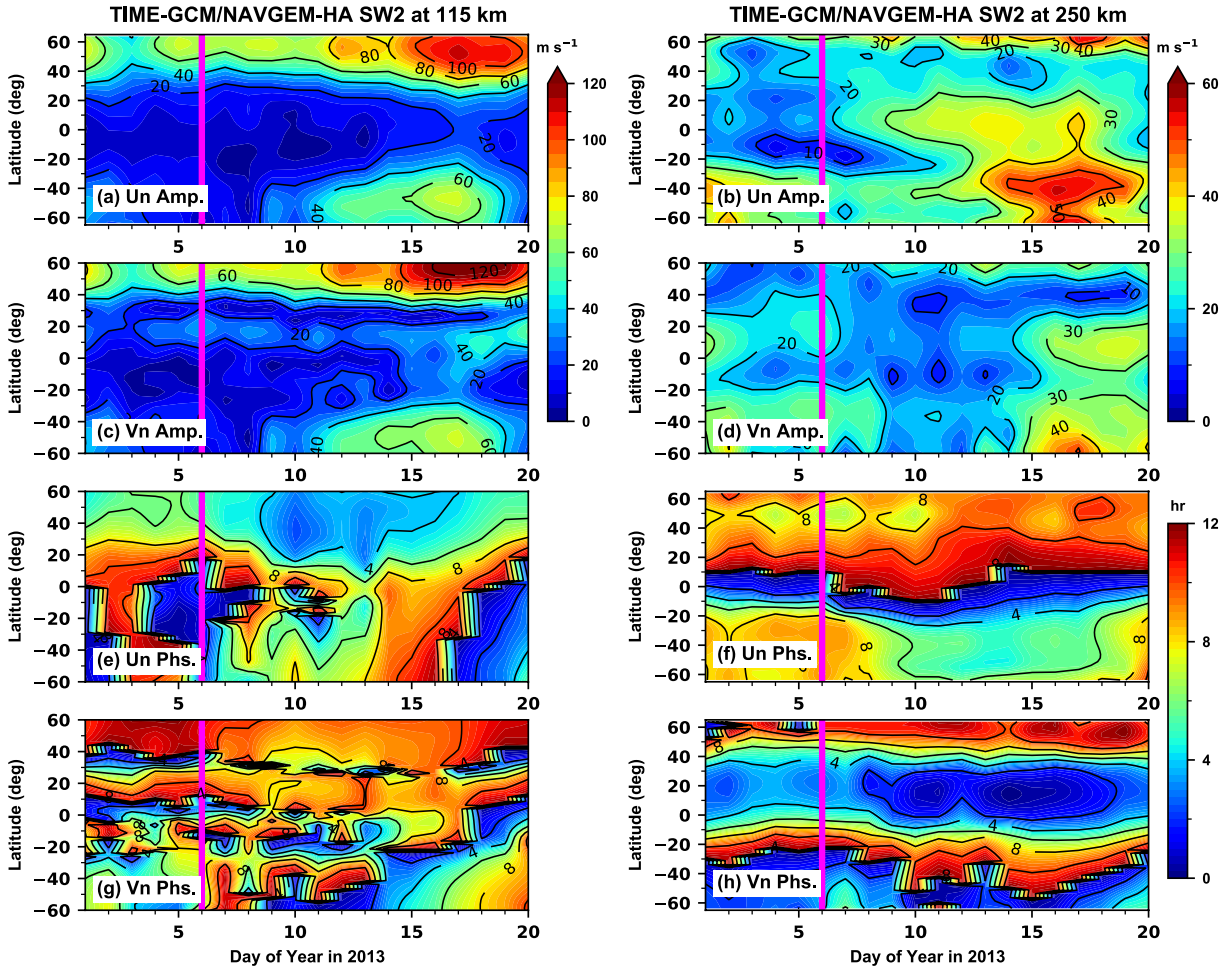

Figure 3. SW2 amplitudes and phases at 115 (left column) and 250 km (right column) as a function of latitude and day of year in 2013. Shown are zonal wind amplitudes (a and b) and phases (e and f) and meridional wind amplitudes (c and d) and phases (g and h). Amplitudes are contoured every ±20 m s^{-1} and phases are contoured every 2 hr. The magenta line marks the day the zonal mean zonal wind reversed at 60°N and 10 hPa.

TIME-GCM reproduce the salient features of the TEC anomalies calculated from observations. Figures 1c and 1d show a general nighttime decrease in TEC over almost all latitudes and UTs illustrated. One notable difference between Figures 1c and 1d is the timing and location of the biggest TEC depletion. TIME-GCM shows this to occur between 20° and 40°S and 0–4 UT, while GNSS TEC observations show a broad TEC depletion between ±40° latitude and 7–11 UT. This spatially broad TEC depletion between 7 and 11 UT is somewhat reproduced in the TIME-GCM, but is slightly weaker than observed. This could potentially be related to the lack of lunar semidiurnal tidal forcing in the TIME-GCM, which is known to have an impact on ionospheric variability during SSWs (N. M. Pedatella & Maute, 2015). Note that the TIME-GCM does not include an explicit lunar potential forcing term in the momentum equations, like N. M. Pedatella et al. (2012) incorporated into WACCM, nor do our simulations include any migrating lunar semidiurnal tidal forcing (M_2) from the GSWM (e.g., N. M. Pedatella & Maute, 2015). Thus, any lunar migrating semidiurnal forcing enters via nudging to NAVGEM-HA analysis/forecast fields in our nudged simulations, but not in the baseline simulation.

To further validate our model results compared to G18, Figure 2 shows observations of TEC at −75° longitude and 8 UT for several days in mid-January in comparison with the GNSS empirical model, and two flavors of TIME-GCM. Specifically, Figure 2a is an adaptation of Figure 4 in G18. Using the definition of "anomalous" TEC values as being either above the 75th percentile or below the 25th percentile and "highly anomalous" as being TEC values outside of either the 90th or 10th percentiles, we see that "highly anomalous" low values of TEC were observed on almost all nights shown following the January 2013 SSW. G18 points out that observed TEC decreased by a factor of 2–4 from "usual" during these nights between an extended range of latitudes from 55°S to 40°N.

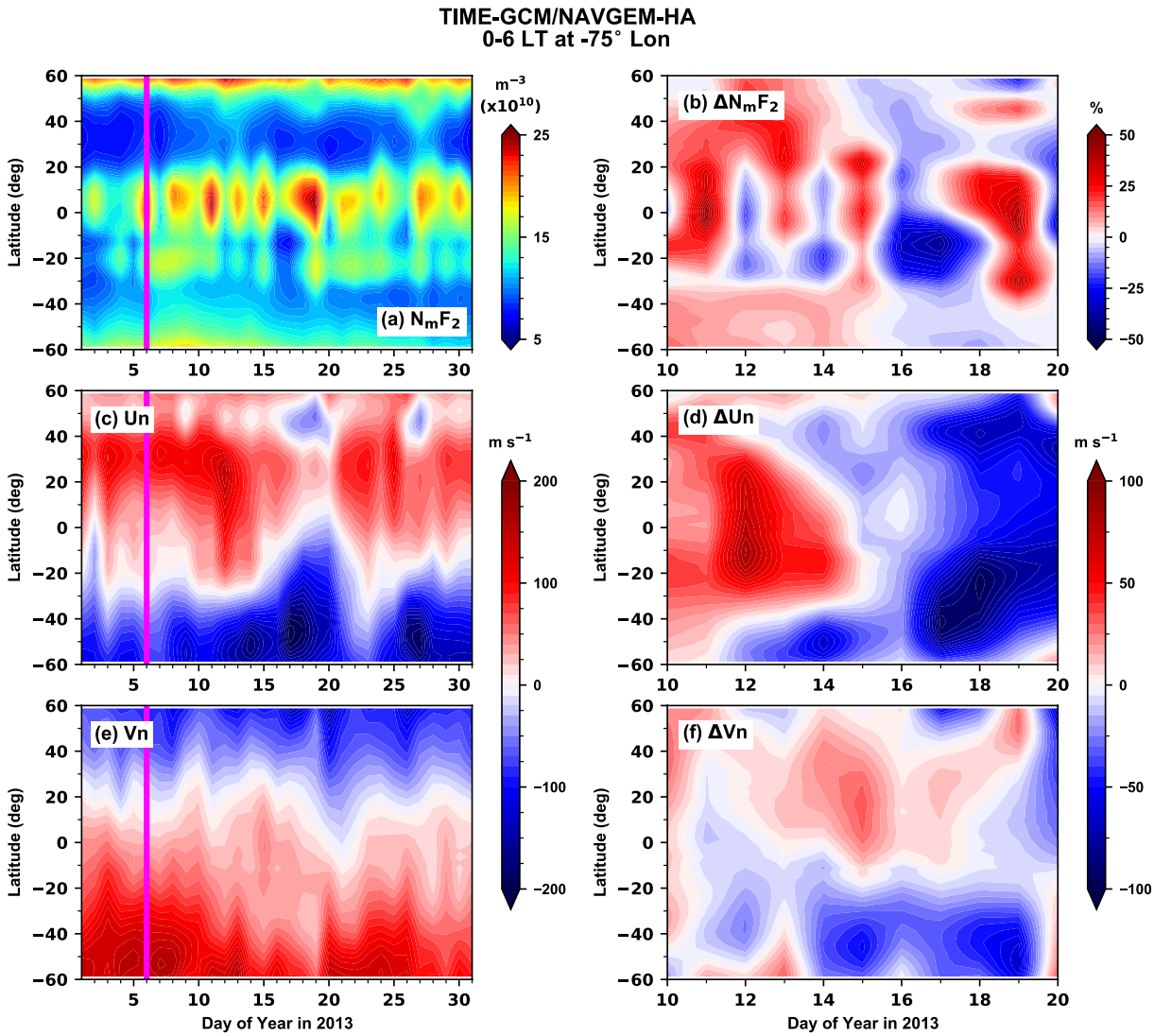

Figure 4. Average N_mF_2 (a), zonal and meridional winds (c and e) from 0 to 6 LT at −75° longitude as a function of day of year in 2013 and latitude from the nudged thermosphere-ionosphere-mesosphere-electrodynamics general circulation simulation at the model level closest to the N_mF_2. The magenta line marks the day the zonal mean zonal wind reversed at 60°N and 10 hPa. Panels (b, d, and f) show N_mF_2 residuals (ΔN_mF_2 in percent), zonal wind residuals (ΔUn), and meridional wind residuals (ΔVn), respectively. Residuals in panels (b, d, and f) are computed relative to their 27-day running mean at each latitude. Note the day of year in 2013 range on the *x*-axis is different between the left and right columns.

Figure 2b shows simulated TIME-GCM TEC values at the same time and location as Figure 2a from the nudged (colored lines) and baseline (gray lines and thick black line) simulations. Comparing the TEC values from the nudged simulation to the average baseline simulation TEC values from 15 to 18 January 2013 we see again that the TIME-GCM reproduces the salient features of the nighttime "ionospheric hole" over mid and low latitudes during the January 2013 SSW when the model is constrained by NAVGEM-HA. Most notably modeled nighttime TEC values decreased by a factor of 2–4 in the nudged simulation compared to the baseline simulation between 35°S and 15°N, which is consistent with GNSS observations and the TEC empirical model. Note that there is an overall low bias in TIME-GCM TEC values compared to observations and the empirical model because TEC is only calculated within the vertical domain of TIME-GCM, which does not take into account topside electron densities above ~500–600 km altitude.

Figures S1 and S2 in Supporting Information S1 provide additional validation of nudged nighttime TIME-GCM electron densities against observations shown in Figures 6–8 of G18 at low and middle latitudes. For example, nudged TIME-GCM qualitatively agrees with observed nighttime electron density depletions in their relative

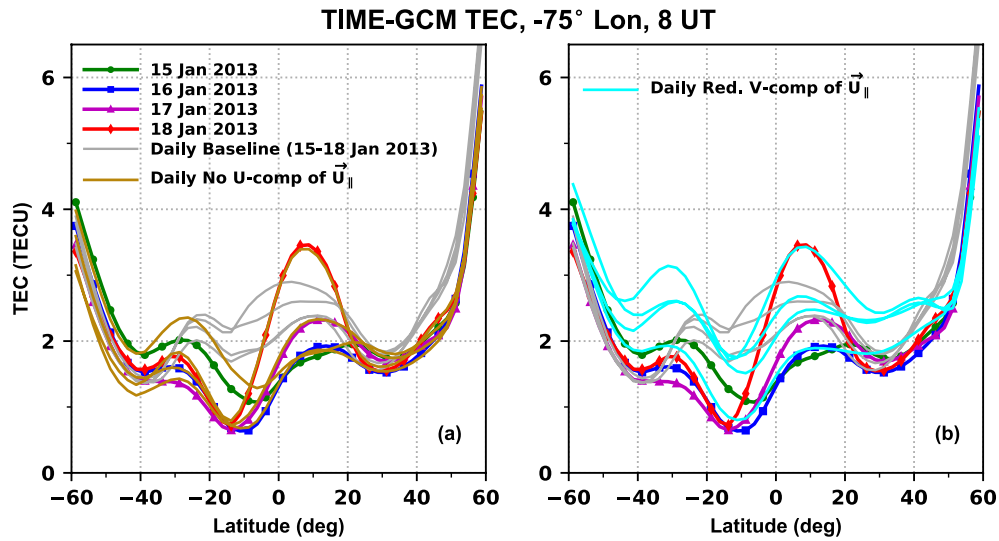

Figure 5. Latitudinal variations of total electron content at −75° longitude and 8 UT (3 LT) simulated by the thermospher e-ionosphere-mesosphere-electrodynamics general circulation (TIME-GCM). Shown in (a) are values from individual nights on 15–18 January 2013 in the nudged (colored lines), baseline (gray line), and nudged no zonal wind contribution to $\overrightarrow{U_{\parallel}}$ (khaki lines) TIME-GCM simulations. Panel (b) is the same as panel (a), except daily nighttime latitudinal profiles are from the nudged TIME-GCM simulation where the meridional wind component of the neutral wind contribution to $\overrightarrow{U_{\parallel}}$ was reduced by a factor of 10 (cyan lines).

magnitudes and timing at selected ionosonde/incoherent scatter radar sites (e.g., Arecibo and Millstone) on the nights of 14, 16, and 18 January 2013. The results in Figures 1 and 2 coupled with those depicted in Figures S1 and S2 in Supporting Information S1 demonstrate that the TIME-GCM is capable of reproducing the observed nighttime ionospheric depletions reported by G18, making these model simulations suitable for diagnosing their cause.

A number of prior studies have confirmed that much of the MLT and TI variability due to SSWs is primarily caused by changes in the vertically propagating wave spectrum, and specifically SW2, as well as the lunar migrating semidiurnal tide (L. P. Goncharenko et al., 2021). G18 stated that it is reasonable to assume SW2 and other tidal modifications during SSWs could affect the nighttime ionosphere by modifying thermospheric neutral winds at *F*-region altitudes (e.g., like N. M. Pedatella et al., 2014; N. M. Pedatella & Maute, 2015, demonstrated in the daytime ionosphere). Therefore, Figure 3 illustrates the SW2 zonal and meridional wind amplitudes and phases at 115 (left column) and 250 km (right column) during the first 20 days of January 2013 from our nudged simulation. Both zonal and meridional wind SW2 amplitudes at 115 km increase at middle northern latitudes at SSW onset, and then see a factor of 2 or more amplitude increase starting around 11 January 2013 at both middle southern and northern latitudes. Similar factor of 2 increases in SW2 zonal and meridional amplitude are simulated at 250 km, an altitude typically located close to the peak electron density in the nighttime ionosphere. These sharp increases in the daily SW2 amplitudes at both 115 and 250 km in Figures 3a–3d occur after the relatively large peak in F10.7 on 11 January 2013, suggesting that such increases at both altitudes are a result of advantageous tidal source and propagation conditions resulting from the SSW (L. P. Goncharenko et al., 2012; Jin et al., 2012; Sridharan et al., 2012).

However, the timing and spatial distribution of these SW2 amplitude increases are slightly different at 250 and 115 km. The presence of SW2 in the middle and upper thermosphere could be forced by Equation 1 lower thermospheric and in situ absorption of EUV; (b) in-situ hydromagnetic coupling due to interaction between diurnally varying winds and ion drag; (c) nonlinear tide-tide interaction between the migrating diurnal and terdiurnal tide; (d) a lower atmospheric source that then vertically propagated into the thermosphere (Angelats i Coll & Forbes, 2002; Forbes, 1982; Jones Jr. et al., 2013). Figure S3 in Supporting Information S1 depicts height-latitude cross-sections of SW2 zonal and meridional wind amplitudes and phases on 16 January 2013. The latitude-altitude cross-sections presented in Figure S3 in Supporting Information S1 indicate that changes in the timing of SW2 amplitude increases and spatial distribution are likely due to viscous dissipation. For example, Lindzen

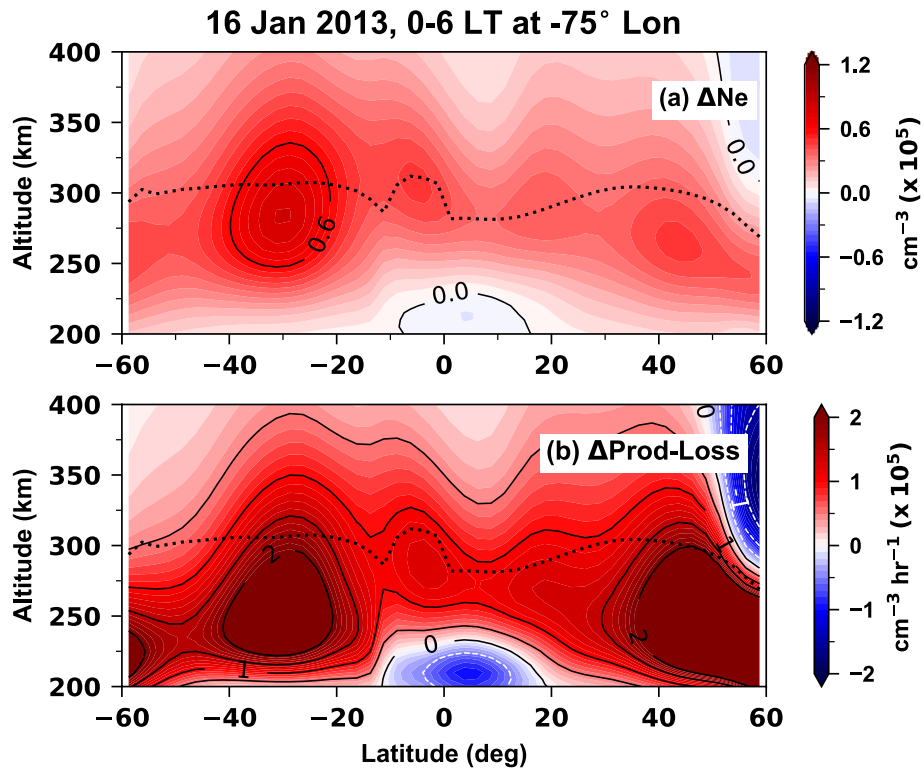

Figure 6. Thermosphere-ionosphere-mesosphere-electrodynamics general circulation (TIME-GCM) simulated changes in the (a) electron density and (b) Prod-Loss at −75° longitude and averaged between 0 and 6 LT on 16 January 2013. Shown are the differences between the nudged TIME-GCM simulation where the meridional wind component of the neutral wind contribution to $\overline{U_{\parallel}}$ was reduced by a factor of 10 and the nudged TIME-GCM simulation where all the O^+ continuity equation terms are unaltered. The dotted line represents the approximate altitudes of the average h_mF_2 from both TIME-GCM simulations.

et al. (1977), Forbes (1982), and Forbes et al. (2022) have demonstrated increased latitudinal broadening of horizontal structures occurs as viscous dissipation increases with altitude, which can be seen in Figures 3a–3d. Simulated SW2 wind amplitudes peak between 110 and 125 km at all low and middle latitudes in Figure S3 in Supporting Information S1, then decrease up to ∼200 km, where finally its amplitude and phase asymptotes to near constant values because molecular dissipation becomes dominant. Since very little SW2 amplitude growth is modeled above ∼200 km in the evanescent-like phase region (i.e., lacking vertical phase progression), we conclude that the SW2 present above ∼200 km is mainly of lower atmospheric origin.

Changes in the SW2 zonal and meridional wind phases are also apparent throughout the thermosphere in response to the January 2013 SSW (Figure 3e–3h). SW2 phase changes in zonal winds of at least ∼3 hr to earlier local times occur at 115 km, 20°–60°N, and at 250 km, 20°–60°S between 10 and 17 January 2013. Changes in the SW2 (and other tidal) phases in the lower thermosphere, modulating the E-region wind dynamo, is the preeminent mechanism used to describe *F*-region ionospheric daytime and tidal variability associated with SSWs (e.g., L. P. Goncharenko, Chau, et al., 2010; N. M. Pedatella et al., 2014; Oberheide, 2022). Meridional wind SW2 phase variations at 115 and 250 km are less obvious than in the zonal winds, but there are some noticeable changes at 115 km and 30°–60°S between 10 and 14 January 2013 (Figure 3g). Also, a 2–3 hr shift in SW2 phase to earlier local times at 250 km and 0°–20°N occurred between 8 and 17 January 2013 (Figure 3h). Lastly, G18 reported that nighttime ionospheric depletions in the American sector occurred later in the night at northern latitudes compared to southern latitudes. The spatiotemporal variability in SW2 horizontal wind amplitudes and phases presented in Figure 3 suggests a possible mechanism to explain the temporal morphology of such nighttime ionospheric anomalies with latitude.

In general, the presence of a thermospheric SW2, with a primarily lower atmospheric source, and simulated wind amplitude and phase variations at 250 km associated with the January 2013 SSW is consistent with the G18

hypothesis; that is, SSW-forced tidal modification of thermospheric winds at *F*-region altitudes are the primary driver of the observed nighttime ionospheric "hole" in the American sector. However, Figure 3 only shows SSW driven changes in a single wave component, whereas the full horizontal wind field is a linear superposition of all waves and tides, as well as the zonal mean. Therefore the left column of Figure 4 shows the peak electron density in the F_2-region ionosphere (N_mF_2) and zonal and meridional winds averaged between 0 and 6 local time (LT) at −75° longitude from our nudged TIME-GCM simulation. The average zonal and meridional winds shown in Figures 4c and 4e are from the constant model pressure level closest to the N_mF_2. Following the stratospheric zonal mean zonal wind reversal on 6 January 2013 (marked by the magenta line in Figure 4), N_mF_2 nighttime depletions at mid-to-low southern latitudes are evident between 15 and 19 January 2013. Coincident with these N_mF_2 nighttime depletions, and SW2 horizontal wind amplitude enhancements in Figure 3, are clear westward wind increases or eastward wind decreases (Figure 4c), and a clear southward shift in the zero meridional wind line from 20°N to 10°S at *F*-region altitudes (Figure 4e). This indicates that SSW-driven *F*-region thermospheric winds variations are present at the same time as the observed nighttime ionospheric depletions in the American sector.

The right column of Figure 4 depicts N_mF_2 and horizontal wind residuals from a 27-day running mean at each latitude, which better highlights concurrent changes between N_mF_2 and the horizontal wind field in TIME-GCM between 10 and 20 January 2013. Given the previously described strong solar flux variations during January 2013, 27-day residuals were taken to filter out ionospheric variations associated with solar rotation effects. Nighttime N_mF_2 values at −75° longitude between 15 and 18 January 2013 are reduced by ∼20%–40% at low latitudes relative to their 27-day running mean values consistent with a clear ionospheric depletion. This nighttime depletion is accompanied by a distinct westward wind anamoly (between 50 and 100 m s^{-1}) at low and middle latitudes, consistent with enhanced SW2 (and other westward propagating waves and tides) momentum deposition at these altitudes (and below). Figure 4f also shows modest SSW-altered meridional wind changes during this same timeframe. Specifically, the magnetic equator at −75° longitude is situated at −12° latitude such that the SSW-induced meridional wind residuals between 14 and 18 January 2013 are enhanced in the poleward direction on either side of the magnetic equator, with residuals ranging from −60 to +40 m s^{-1} at low and middle latitudes.

Note that on 17 January 2013 Kp was elevated to 4, which also led to increased equatorward and westward neutral winds (Fashae et al., 2022; Maute et al., 2015; Ribeiro et al., 2019) and could contribute to the neutral wind residuals illustrated in Figure 4. However, Figure S4 in Supporting Information S1 illustrates nighttime TI conditions in the American sector from nudged TIME-GCM simulations performed by Jones Jr. et al. (2020) during January 2013 where the solar and geomagnetic inputs were held fixed at F107 values of 130 sfu and Kp ≃ 1, respectively. The spatiotemporal variations in N_mF_2, horizontal winds, and their residuals illustrated in Figure S4 in Supporting Information S1 are extremely similar (i.e., in magnitude, direction, and timing) to those shown in Figure 4, demonstrating the prevalent SSW influence on the nighttime TI in the American sector. A notable exception when geomagnetic effects could be influencing the nighttime F-region can be seen in Figure 4 at northern middle latitudes, where electron density decreases are more pronounced and westward zonal wind residuals are larger than those shown in Figure S4 in Supporting Information S1. Nonetheless, we will show later that similar zonal and meridional wind residuals exist for other SSWs during weaker geomagnetic activity levels, further indicating that these neutral wind residuals are preferentially responding to SSW forcing of the TI.

Given the results depicted in the right column of Figure 4 it is unclear which component of the horizontal wind (i.e., zonal or meridional) is primarily responsible for altering the nighttime ionosphere. Zonal wind induced electron density changes in the ionosphere are dependent on both the sign of the zonal wind and the magnetic declination angle (S.-R. Zhang et al., 2012). The parallel ion drift $V^{\parallel}_{zonal}$ (positive upward along the magnetic field lines) induced by thermospheric zonal winds U_e (positive for eastward winds), $V^{\parallel}_{zonal} = -U_e \sin D \cos I$, is either upward or downward perturbation depending on the sign of the declination angle *D* and direction of the zonal wind (*I* is the magnetic inclination angle). With the exception of high southern latitudes ($\lessapprox$50°S), the magnetic declination along −75° longitude is negative, and a more westward wind (Figures 4b and 4d) driven by the enhanced SW2, would lead to a downward perturbation along the magnetic field lines. Since the nighttime ionosphere is strongly controlled by chemical and transport processes, downward plasma motion would lead to lower electron density due to increased recombination rates at lower altitudes. Also, thermospheric meridional winds are well known to be an efficient driver of electron density changes through forcing field-aligned plasma motions. For example, poleward winds act to push plasma down magnetic field lines, leading to shorter chemical lifetimes of electrons and more loss.

In order to diagnose the primary driver of this nighttime ionospheric depletion we analyzed the fundamental forcing terms in the O^+ continuity equation. In TIME-GCM the ion continuity equation is given by the following:

$$\frac{\partial N_i}{\partial t} = q - \beta N_i - \nabla \cdot \left(N_i \vec{V_i} \right) \tag{1}$$

In Equation 1, N_i is the O^+ number density, q is the production rate, β is the loss coefficient, and $\vec{V_i} = \vec{V_\perp} + \vec{V_\parallel}$, where the symbols $\perp$ and $\parallel$ represent the ion velocity component perpendicular and parallel to the magnetic field line, respectively. Roble et al. (1988) defines the perpendicular ion velocity as $\vec{V_\perp} = \frac{\vec{E} \times \vec{B}}{|B|^2}$, and the parallel ion velocity as $\vec{V_\parallel} = \vec{U_\parallel} - \frac{1}{\nu_{in}} \left[\vec{g_\parallel} - \frac{\nabla_\parallel (P_e + P_i)}{\rho_i} \right]$, where $\vec{B}$ is the magnetic field, $\vec{E}$ is the electric field, $\vec{U}$ is the neutral wind, ν_{in} is the ion-neutral collision frequency, $\vec{g}$ is the gravitational acceleration, P_e and P_i are the electron and ion pressures, respectively, and ρ_i is the ion mass density. The time rate of change of O^+ number density in TIME-GCM is determined by production (first term on the right hand side of Equation 1), loss (second term on the right hand side of Equation 1), and transport (third term on the right hand side of Equation 1). The transport term can be further broken down into transport by the $\vec{E} \times \vec{B}$ plasma drift, neutral wind transport, and ambipolar diffusion. Adopting the naming convention initially used by Lei et al. (2008), and more recently used by N. M. Pedatella et al. (2014), J. Liu et al. (2016), and G. Lu et al. (2020) the time rate of change of O^+ number density can be written as:

$$\frac{\partial O^+}{\partial t} = Prod. - Loss + Amb\_diff + Trans\_wind + Trans\_E \times B \tag{2}$$

To isolate the effects of the SSW-altered thermospheric horizontal winds on nighttime ionospheric electron density we performed a sequence of additional nudged TIME-GCM simulations. First we performed a TIME-GCM simulation where the zonal component of the neutral wind contribution to $\vec{U_\parallel}$ in the *Trans_wind* term was set to zero. Figure 5a illustrates the simulated latitude profiles of TEC at −75° longitude and 8 UT (3 LT) on several nights in January 2013. The different colored (i.e., green, blue, magenta, and red) profiles are from the nudged simulation, while the gray lines are from the same nights (15–18 January 2013), but from the baseline TIME-GCM. Comparing the TEC values from the nudged simulation to the average baseline simulation (i.e., simulation with climatological tides and background middle atmosphere) TEC values from 15 to 18 January 2013 we see that the TIME-GCM reproduces the salient features of the nighttime ionosphere over mid and low latitudes during the January 2013 SSW when the model is constrained by NAVGEM-HA. The individual khaki-colored traces in Figure 5a are TEC latitudinal profiles for individual nights in January 2013, but from the nudged TIME-GCM simulation with zonal component of the neutral wind contribution to $\vec{U_\parallel} = 0$. Setting the SSW-modulated zonal wind contribution to $\vec{U_\parallel} = 0$ in the O^+ continuity equation does not have much of an effect on the nighttime ionosphere. This indicates the S.-R. Zhang et al. (2012) mechanism proposed by G18 is not the primary driver of the nighttime ionospheric depletions during the January 2013 SSW.

Figure 5b is the same as Figure 5a, except the cyan colored lines represent latitudinal variations of TEC from the nudged TIME-GCM simulation where the meridional wind component of the neutral wind contribution to $\vec{U_\parallel}$ was reduced by a factor of 10. Note that the neutral wind contribution to $\vec{U_\parallel}$ was reduced by a factor of 10 instead of setting it zero as was done for the zonal wind case for model stability purposes. For almost every night, at latitudes between ±50°, clear increases on the order of 50% in nighttime TEC occur relative to the unaltered nudged simulation. This indicates that the changes in the *F*-region meridional wind resulting from SSW-altered dynamics are strongly contributing to the nighttime ionospheric depletions observed by G18 and modeled herein. Although not shown here, we performed two analogous simulations using nudged TIME-GCM thermospheric fields to drive the SAMI3 ionospheric model (Sami3 is Another Model of the Ionosphere, see Huba et al., 2000; Huba et al., 2008). These SAMI3 simulations wherein the neutral zonal or meridional wind contributions to the parallel to $\vec{B}$ charged particle motion above 150 km were switched off in all seven ion species were performed to assess the veracity of our TIME-GCM simulations. TIME-GCM driven SAMI3 simulations produced very similar results to those shown by the nudged TIME-GCM alone in Figure 5; that is, the zonal wind contribution to the field aligned plasma motion does little to alter the *F*-region electron density during the January 2013 SSW, while removing the poleward meridional wind contribution to the field aligned plasma motion acts to increase nighttime plasma densities in the *F*-region ionosphere.

Figure 6 shows changes in the electron density and production-loss term in Equation 2 on 16 January 2013 averaged between 0 and 6 LT at −75° longitude. These changes in electron density and chemistry were computed

between the nudged TIME-GCM simulation where the meridional wind component of the neutral wind contribution to $\overrightarrow{U_{\parallel}}$ was reduced by a factor of 10 and the nudged TIME-GCM simulation where all the O^+ continuity equation terms are unaltered. Approximate average altitudes of the F_2-region peak electron density height (h_mF_2) are illustrated by the dotted lines in Figure 6 for reference. As expected from the results shown in Figure 5, electron densities in almost the entire F-region are larger when the meridional wind contribution to $\overrightarrow{U_{\parallel}}$ is significantly reduced during the January 2013 SSW. Reducing the down magnetic field line transport perturbations of O^+ should result in a net increase in the production-loss since O^+ has a longer chemical lifetime at higher altitude. Figure 6b illustrates exactly this scenario, whereby decreased down magnetic field line transport leads to a positive net change in the O^+ production-loss term, further emphasizing the role of thermospheric meridional wind modification during the January 2013 SSW in forcing the observed nighttime depletions in the American sector. Note that by altering the *Trans_wind* term in Equation 2, one could expect nonlinear feedbacks in the simulated neutral zonal and meridional winds due to changes in ion drag. However, these neutral wind changes via nonlinear feedbacks to the ion drag forcing in the neutral horizontal momentum equations are relatively small (e.g., wind changes on the order of 20–30 m s^{-1} or 10%–15% of the values in Figure 4), thereby having little impact on our force term analysis presented above in Figures 5 and 6.

We now turn our attention to quantifying the role of enhanced SW2 forcing on the thermospheric wind field during the January 2013 SSW. Figure 7 shows latitudinal TEC profiles on the nights with significant ionospheric depletions simulated by the TIE-GCM including (Figure 7a, All Waves) and excluding (Figure 7b, w/o SW2, colored lines) SW2 forcing at the model lower boundary from our nudged TIME-GCM/NAVGEM-HA simulation. For climatological context, daily latitudinal TEC profiles from a baseline TIE-GCM simulation are represented by the gray lines of Figure 7b. When the TIE-GCM is forced with TIME-GCM/NAVGEM-HA fields at the model lower boundary it does reproduce the salient nighttime ionospheric features in both the observations of G18, and the nudged TIME-GCM, including the ionospheric "hole." By removing SW2, nighttime TEC values at low and middle latitudes generally increase by at least ∼50%, with TEC increases as high as a factor of 2 in some places (e.g., 10°S on 17 January 2013, magenta line in Figure 7b). However, excluding the SSW-enhanced SW2 alone does not increase TEC values to the climatological values computed in the baseline TIE-GCM simulation, and at some locations, removing SW2 decreases the TEC (e.g., red line in Figure 7b near the equator). This suggests that other SSW-altered wave perturbations also play a role in reducing nighttime ionospheric plasma densities (e.g., the westward propagating semidiurnal non-migrating tides with zonal wave numbers 1 and 3 Fang et al., 2012; Maute et al., 2015; Pancheva et al., 2009; N. Pedatella, 2022).

Figure 8 further elucidates the role of enhanced SW2 forcing on the thermospheric winds during the January 2013 SSW event. Shown are the N_mF_2, zonal and meridional wind residuals relative to their 27-day running mean values averaged between 0 and 6 LT at −75° longitude from TIE-GCM simulations with (left column) and without (right column) SW2 forcing at the lower boundary from nudged TIME-GCM. When the full wave spectrum from the nudged TIME-GCM simulation is included at the TIE-GCM lower boundary clear nighttime depletions of 50% or more exist in the nighttime F-region ionosphere between 15 and 17 January 2013 (Figure 8a), whereas these depletions are significantly reduced when SW2 forcing is not included at the TIE-GCM lower boundary (Figure 8b). Westward wind residuals at F-region altitudes are also significantly reduced between 15 and 20 January 2013, in the absence of SW2 lower boundary forcing in the TIE-GCM. Specifically, comparing Figure 8c to Figure 8d, we see that westward zonal wind residuals are reduced by about half, or 30–40 m s^{-1}, between ±50° latitude on the nights of 17–20 January 2013. At the same time, in the "w/o SW2" TIE-GCM simulation poleward meridional wind residuals are also reduced by about half, or ±20 m s^{-1}, between ±50° latitude. Taken together, the TIE-GCM modeling results shown in Figures 7 and 8 indicate that the SSW-driven enhancements of the vertically propagating SW2 are the preeminent driver of thermospheric wind modifications at F-region altitudes during the January 2013 SSW.

3.2. Modeling and Observations During Other SSWs

G18 also extended their observational analysis to the minor SSWs of January 2008 and 2012 and attempted to determine if similar nighttime ionospheric depletions occurred in the American sector during these events. They concluded that similar, but weaker nighttime ionospheric depletions were present during the minor SSW of January 2008, but results during the minor SSW of January 2012 were inconclusive due to enhanced solar and geomagnetic activity coincident with the timing of the SSW. Thus, this section not only further attempts to assess

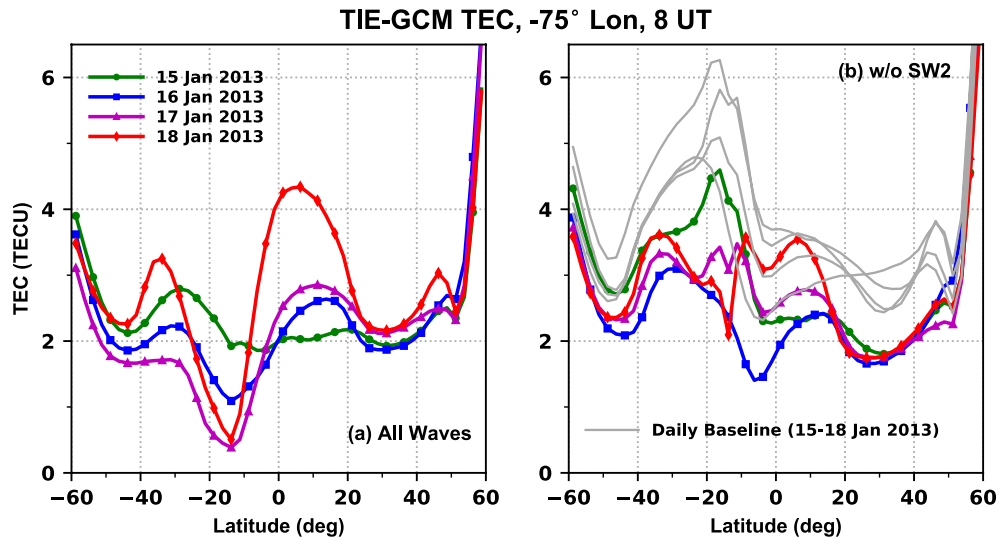

Figure 7. Latitudinal variations of total electron content (TEC) at −75° longitude and 8 UT (3 LT) simulated by the thermosphere-ionosphere-electrodynamics general circulation (TIE-GCM). Shown in (a) are values from individual nights on 15–18 January 2013 from a TIE-GCM simulation where the model lower boundary was forced by full fields from a thermosphere-ionosphere-mesosphere-electrodynamics general circulation/high-altitude version of the Navy Global Environmental Model (TIME-GCM/NAVGEM-HA) simulation (colored lines). Panel (b) is the same as panel (a), except daily nighttime latitudinal profiles are from a TIE-GCM simulation where the SW2 at the model lower boundary was removed from TIME-GCM/NAVGEM-HA fields (colored lines). Also shown in panel (b) are daily TEC profiles from a baseline TIE-GCM simulation.

the presence of nighttime ionospheric depletions in the American sector associated with other SSWs, but also to determine if such ionospheric depletions do exist, whether they are driven by thermospheric wind changes due to vertically propagating tides.

3.2.1. January-February 2010 SSW

Middle atmospheric and space weather conditions during the January-February 2010 SSW were previously described by L. P. Goncharenko, Hsu, et al. (2013) (Figure 1), Paes et al. (2014) (Figure 7), McCormack et al. (2017) (Figure 1), Wu and Nozawa (2015) (Figure 1), and Jones Jr. et al. (2018) (Figure 3). To briefly summarize, space weather conditions during January-February 2010 were typical of solar minimum and geomagnetically quiet conditions (i.e., daily F10.7 values were less that 90 sfu, and with the exception of a few days Kp values were less than 4). Middle atmospheric conditions during January-February 2010 were more complex compared to the January 2013 event. High northern latitude stratospheric temperatures at 10 hPa increased by ∼40 K between 18 and 22 January 2010, and high northern latitude middle atmospheric zonal mean zonal winds started to reverse from eastward to westward around the same time, and remained westward in the stratosphere and mesosphere into early February. Specifically, mean zonal winds at 60°N and 10 hPa did not turn westward until 9 February 2010, thereby not reaching the classical major SSW classification of Butler et al. (2015) until then. However, for the purposes of this study, between mid-January and mid-February 2010 should be considered as the time period when the middle atmosphere was disturbed compared to climatology.

Figures 9a and 9b show TEC from the nudged and baseline TIME-GCM simulations, respectively, on 4 February 2010 at −75° longitude as a function of latitude and 0–12 UT (19-7 LT). Although TEC values are low in the baseline simulation, they are even lower in the nudged simulation, similar to Figure 1 during the January 2013 SSW event. Specifically, Figure 9c illustrates that between 2 and 4 UT and 30°–60°S, and between 4 and 10 UT and 20°S–0° the $TEC_{Nudge}/TEC_{Baseline}$ is less than 0.5, with ratios reaching as low as 0.1. These exceptionally low nudge-to-baseline TEC ratios displayed in Figure 9 are also consistent with those in shown in Figure 1 during the January 2013 SSW event.

Figure 9d depicts the data-to-empirical model ratio for GNSS TEC at the same date, location, and time as our TIME-GCM results. Similar to January 2013, the TIME-GCM generally agrees well with the observed TEC

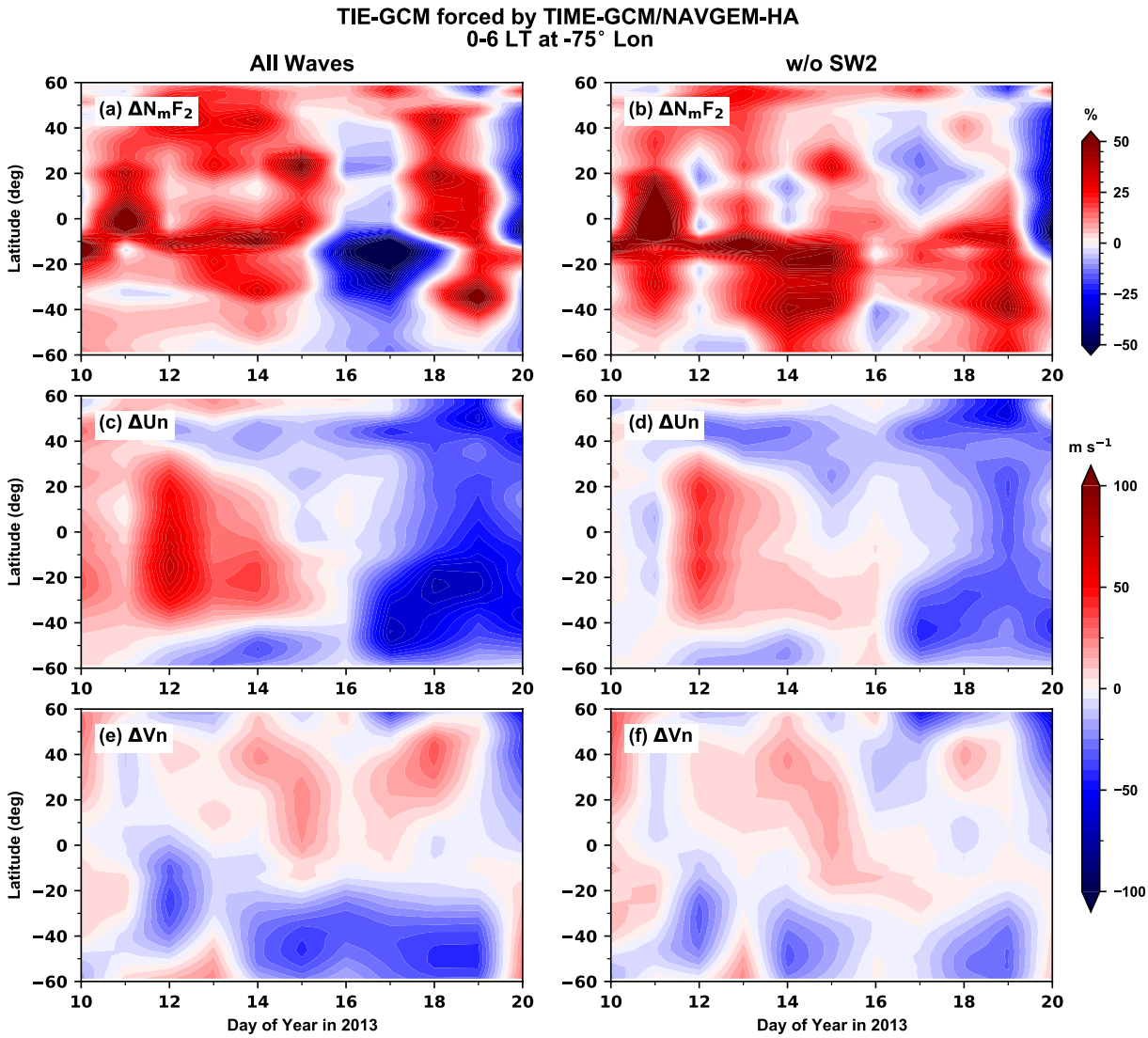

Figure 8. N_mF_2 residuals (ΔN_mF_2 in percent (a and b), zonal wind residuals (ΔUn (c and d)), and meridional wind residuals (ΔVn (e and f)) relative to their 27-day running mean at each latitude from 0 to 6 LT at −75° longitude as a function of day of year in 2013 from thermosphere-ionosphere-electrodynamics general circulation model simulations with (left column, "All Waves") and without (right column, "w/o SW2") SW2 forcing at the model lower boundary from nudged thermospher e-ionosphere-mesosphere-electrodynamics general circulation. Zonal and meridional wind residuals are computed at the model level closest to the electron density peak.

anomalies, though with some differences. Overall, observed TEC values on 4 February 2010 are lower than those from the empirical model, reaching values of 0.4 or lower between 7 and 10 UT at tropical latitudes, indicative of a significant decrease in TEC at night in the American sector. Figure S5 in Supporting Information S1 also shows that between 3 and 5 February 2010 observed TEC values were at least anomalous to highly anomalous using the G18 definition (i.e., below the 25th or 10th percentile, respectively) compared to the empirical model. Therefore, we conclude that not only was there a deep ionospheric hole in the American sector on several nights during the January-February 2010 SSW, but also that the nudged TIME-GCM is capable of reproducing the salient ionospheric features during this event.

To understand if the February 2010 deep ionospheric depletion shares a common forcing mechanism to that of the January 2013 deep ionospheric depletion Figure 10 shows the N_mF_2, zonal, and meridional winds averaged between 0 and 6 LT and their residuals from a 27-day running mean at each latitude at −75° longitude from mid-January to mid-February 2010. Note the average zonal and meridional winds shown in Figures 10c–10f are from the model level closest to the N_mF_2. The solid magenta line on 9 February 2010 (day of year 40) marks the day where the zonal mean zonal wind reversed at 60°N and 10 hPa signifying a major SSW after Butler

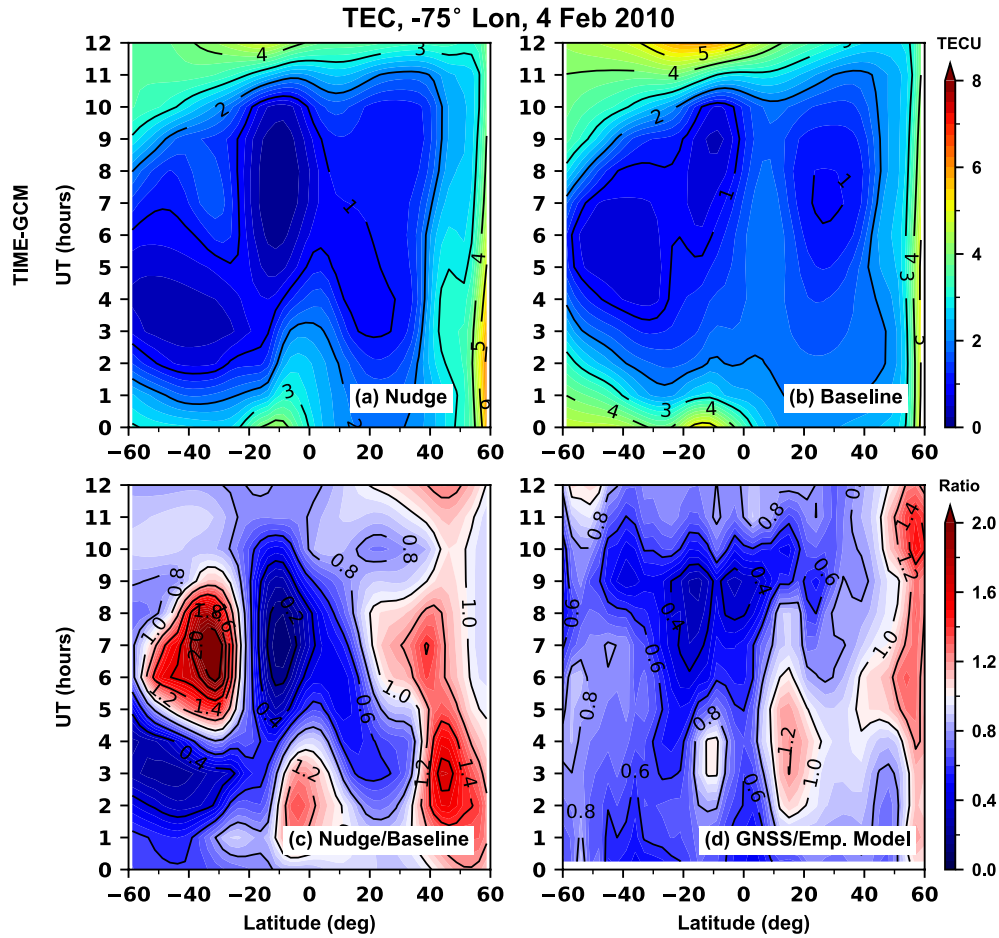

Figure 9. Same as Figure 1, except for 4 February 2010.

et al. (2015). However, McCormack et al. (2017) states, for SSW events, a sustained reversal (>5 days) of mesospheric zonal winds at 60°N typically precedes the stratospheric wind reversal, and this sustained mesospheric zonal wind reversal better relates tidal variability to MLT variability. This is marked by the black dotted vertical line on 27 January 2010 (day of year 27).

Figures 10a and 10b reveal large ionospheric depletions at low and middle latitudes between 1 and 6 February 2010. Nighttime N_mF_2 residuals at −75° longitude between 1 and 6 February 2010 show values 30%–60% lower than their 27-day running mean values, suggesting that the ionospheric hole during the January-February 2010 SSW was potentially deeper than the one associated with the January 2013 SSW. Similar to the January 2013 ionospheric depletion, Figures 10c and 10d show notable increased westward zonal wind anomalies on the order of 50–100 m s^{-1} at low and middle latitudes between 1 and 8 February 2010 in the *F*-region. The timing of these enhanced westward zonal wind anomalies in the *F*-region are consistent with increased horizontal wind amplitudes of SW2, as well as SW1 and SW3, in the MLT region reported in Figure 7 of Wu and Nozawa (2015) and Jones Jr. et al. (2018). Further, *F*-region meridional winds in Figure 10e exhibit a striking disruption between 1 and 8 February 2010, with meridional winds changing from convergent (i.e., equatorward winds) to divergent (i.e., poleward) near the equator. Meridional wind residuals during this timeframe range from −70 to +40 m s^{-1} in Figure 10f.

The results in Figure 10 all indicate that a similar mechanism is responsible for driving the deep nighttime ionospheric depletions in the American sector during both the January-February 2010 and January 2013 SSW. That is, enhanced tidal forcing in response to a SSW acts to modify *F*-region horizontal winds, which then greatly reduces the nighttime ionospheric electron densities, via neutral wind driven magnetic field aligned plasma motion. Comparing meridional wind residuals (Figure 10f) with N_mF_2 residuals (Figure 10b) signifies that the

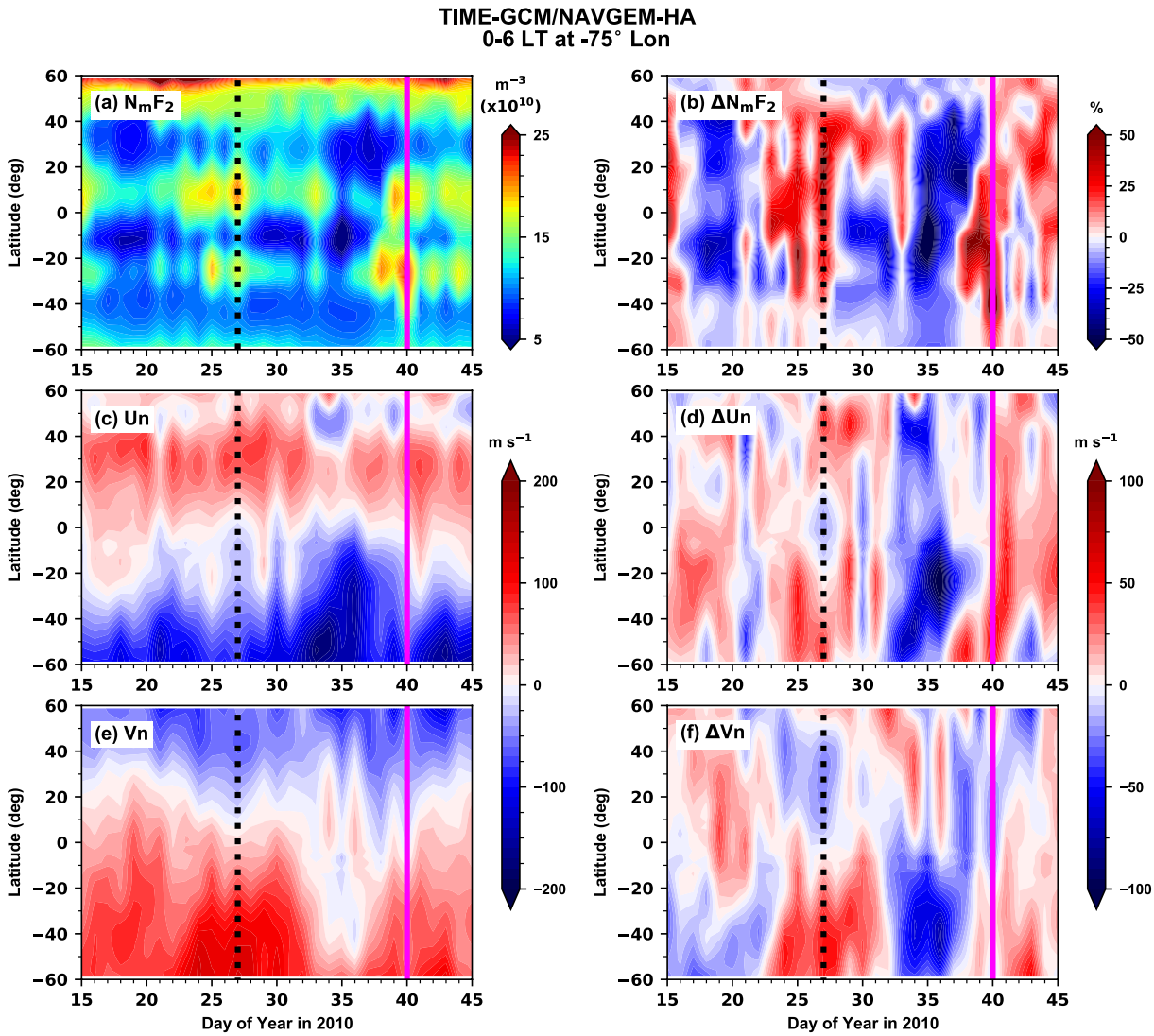

Figure 10. Same as Figure 4, except from 15 January to 14 February 2010. The black dotted line marks the onset (27 January 2010) of persistent mesospheric winds reversals at 60°N as defined by McCormack et al. (2017), while the magenta line mark the day (9 February 2010) the zonal mean zonal wind reversed at 60°N and 10 hPa.

nighttime ionospheric depletions in the American sector during January-February 2010 are more readily forced by meridional winds than zonal winds. For example, nighttime depletions in N_mF_2 occur between day of year 16–20 and between 34 and 37 in 2010, when meridional wind residuals are primarily poleward, whereas nighttime enhancements in N_mF_2 occur between day of year 23–27, when meridional wind residuals are equatorward. This type of oscillatory behavior in N_mF_2 residuals is also suggestive of tidal modulation by planetary waves during SSWs (e.g., N. M. Pedatella & Liu, 2013).

Figure 11 shows latitudinal TEC profiles on the nights with significant ionospheric depletions simulated by the TIE-GCM including (Figure 11a, All Waves) and excluding (Figure 11b, w/o SW2, colored lines) SW2 forcing at the model lower boundary from our nudged TIME-GCM/NAVGEM-HA simulation. For climatological context, daily latitudinal TEC profiles from a baseline TIE-GCM simulation in February 2010 are represented by the gray lines of Figure 11b. Differences between the colored latitudinal profiles in Figures 11a and 11b highlight the impact of SW2 on generating the nighttime electron density depletions during the January-February 2010 SSW. By removing SW2 at the TIE-GCM lower boundary, nighttime TEC in the American sector generally increases at tropical latitudes by 50% or more, comparable to the results shown in Figure 7 for the January 2013 SSW. This is particularly evident on the night of 4 February 2010, where TEC values shift by 1 or more TECU.

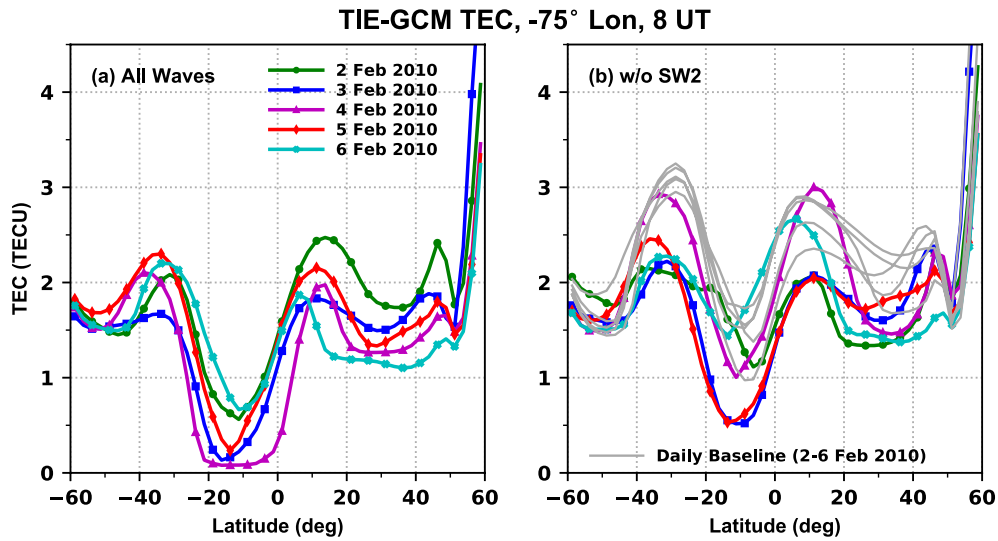

Figure 11. Same as Figure 7, except from 2 to 6 February 2010.

While excluding the SSW-enhanced SW2 at the TIE-GCM lower boundary does increase nighttime TEC values compared to the simulations that include SW2 lower boundary forcing, TEC values in the w/o SW2 case are still smaller relative to climatological TIE-GCM values (see gray 'baseline' traces in Figure 11b), suggesting other waves and tides also play a role in modifying the nighttime ionosphere.

3.2.2. January 2021 SSW

Recent studies by N. Pedatella (2022), Oberheide (2022), and R. Zhang et al. (2022) reported the observed and modeled variability during the January 2021 SSW. Both N. Pedatella (2022) and Oberheide (2022) described the impacts of SSW-enhanced SW2 (and other tidal components) in forcing the TEC variability observed by COSMIC-2, while R. Zhang et al. (2022) suggested the importance of *F*-region meridional wind changes in driving aberrant magnetic field-aligned plasma motion. However, these recent works did not specifically focus on nighttime ionospheric depletions in the American sector. Figure 12 illustrates middle atmospheric, ionospheric, and thermospheric conditions between 22 December 2020 and 20 January 2021. Focusing first on the lower and middle atmospheric variability, sharp northern high latitude temperature increases commenced on 1 January 2021, while the zonal mean zonal winds at 60°N reversed throughout the entire stratosphere and mesosphere in early January (Figures 12a and 12b). Zonal mean zonal winds at 10 hPa and 60°N ultimately reversed direction on 5 January 2021, signifying an onset of a major SSW (Butler et al., 2015). Stratospheric (and mesospheric, see N. Pedatella, 2022) zonal mean zonal winds remained relatively weak throughout the entire month of January due to tropospheric forcing conditions (see Q. Lu et al., 2021; Rao et al., 2021). In spite of this, N. Pedatella (2022) showed that it was only during the initial zonal mean zonal wind reversal in early January 2021 where zonal mean zonal winds reversed throughout the middle atmosphere, while zonal mean zonal winds in the upper stratosphere and mesosphere remained eastward during later zonal mean zonal wind reversals at 10 hPa and 60° N. Solar and geomagnetic forcing were indicative of solar minimum and geomagnetically quiet conditions, with daily F10.7 values less than 90 sfu and Kp values only periodically reaching a value of 4.

The nighttime ionospheric electron densities at −75° longitude and 260 km and averaged between 0 and 6 LT are shown in Figure 12c, and illustrate the ionospheric response to the January 2021 SSW. Concurrent with the appearance of westward winds in the middle atmosphere from MERRA2 are sharp decreases in the nighttime electron densities in the American sector from COSMIC-2/GIS data. Figure 12d shows electron density residuals at the same time, longitude, and altitude from COSMIC-2/GIS and reveal depletions of up to 50%–70% relative to their 27-day running mean values. Note that ionospheric variability can be driven by only minor variations in geomagnetic activity (e.g., Cai et al., 2021) such as those shown in Figures 12i and 12j, and in fact, modeling from N. Pedatella (2022) does indicate a contribution from solar and geomagnetic activity to the observed ionospheric variability during the 2020–2021 boreal winter months. However, N. Pedatella (2022) do demonstrate that observed mean ionospheric depletions in the first half of January 2021 are generally reproduced in the

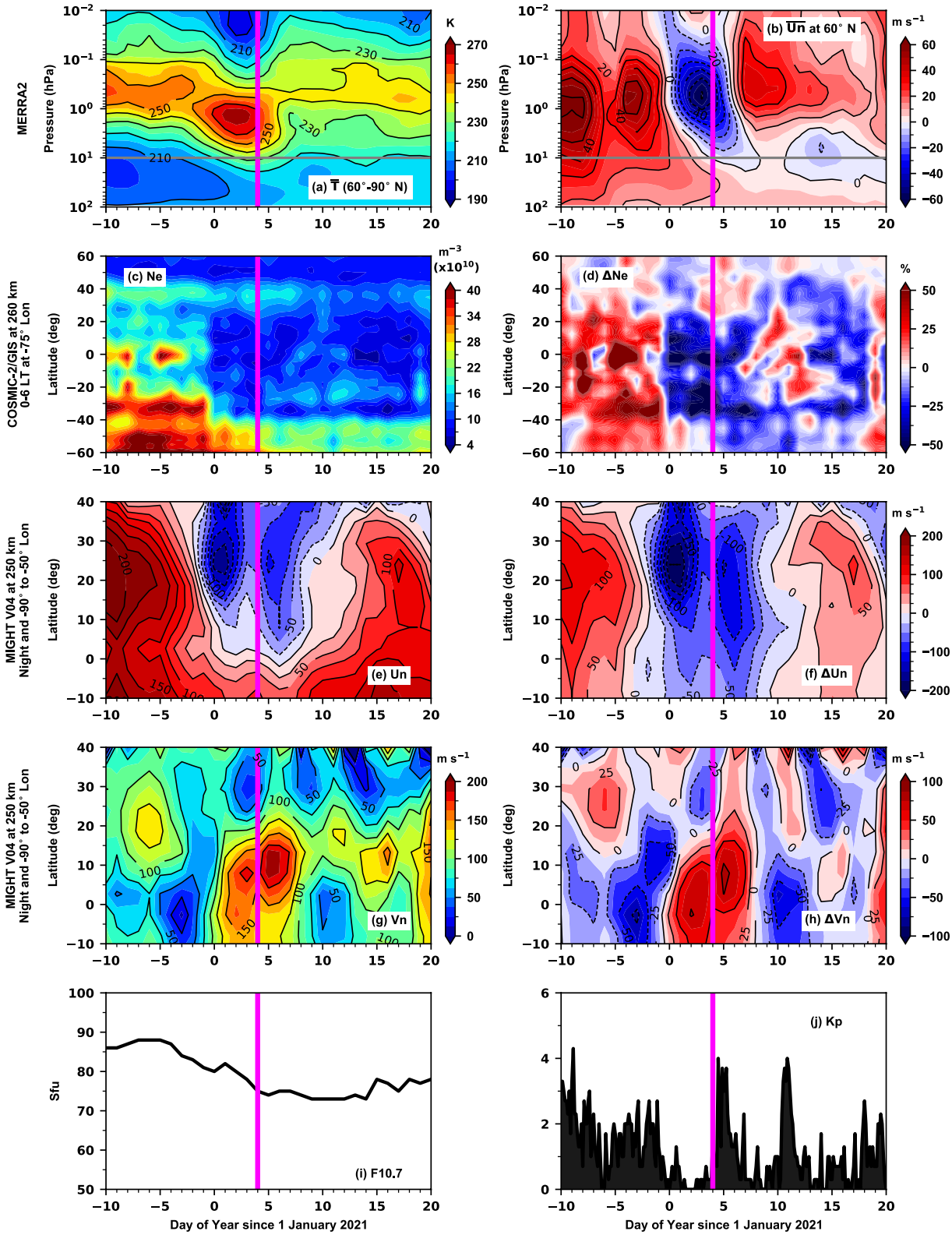

Figure 12. Variability in the zonal, diurnal, and cosine-weighted mean temperatures between 60° and 90°N from MERRA2 (a), zonal and diurnal mean zonal winds at 60°N from MERRA2 (b), electron density at 260 km and −75° longitude averaged between 0 and 6 LT from COSMIC-2/GIS (Ne, (c)), mean nighttime (18–24 and 0–6 LTs) zonal (e) and meridional (g) winds at 250 km averaged between −90° to −50° longitude from MIGHTI, F10.7 cm solar flux (i), and geomagnetic Kp index (j) during the 2020–2021 SSW. Also shown are 27-day running mean residuals at each latitude in COSMIC-2/GIS electron density (ΔNe, (d)), as well as MIGHTI zonal (ΔUn, (f)) and meridional (ΔVn, (h)) winds. The magenta line marks the day (5 January 2021) the zonal mean zonal wind reversed at 60°N and 10 hPa.

absence of solar flux and Kp variations. Oberheide (2022) also made similar considerations observationally. This suggests that the deep nighttime ionospheric depletions in the COSMIC-2/GIS data are associated with SSW forcing the MLT and TI system.

Figures 12e–12h depict the mean nighttime (i.e., 18–24 and 0–6 LT) horizontal winds and their residuals between −90° to −50° longitude, 10°S to 40°N and at 250 km, as observed by the MIGHTI instrument. Remarkably, the same *F*-region horizontal wind structure and variations are observed by MIGHTI during the January 2021 SSW as was simulated by the nudged TIME-GCM for the January-February 2010 and January 2013 SSWs. Namely, nearly coincident with upper stratospheric and mesospheric zonal mean zonal wind reversals and nighttime ionospheric depletions, we see a reversal in the *F*-region zonal winds from eastward to westward, and increased poleward flow in the *F*-region meridional winds. Raw westward (northward) wind values reach up to −150 m s^{-1} (150 m s^{-1}) in Figure 12e (12g), with 27-day running mean residuals reaching values of ±75 m s^{-1} between 1 and 9 January 2021. Note that we estimate ICON local time precession effects on the calculated wind variations are on the order of ±25 and ±45 m s^{-1} in the zonal and meridional winds, respectively (Figure 12). These local time precession effects are still well below the 100–200 m s^{-1} raw horizontal winds, and 27-day running mean residuals that reach magnitudes of up to 80 m s^{-1} or more. Also, note that we cannot conclusively exclude effects from concurrent geomagnetic activity, especially on the *F*-region neutral winds. But, based on constant solar and geomagnetic forcing simulations discussed earlier for January 2013 (see Figure S4 in Supporting Information S1) and January-February 2010 (not shown), we suspect these geomagnetic effects on the observed *F*-region variability are likely of secondary importance compared to the SSW effects (especially since Kp values never get much above 4).

The timing in the zonal and meridional wind changes depicted in Figure 12 are consistent with enhancements in the observed semidiurnal tides from MIGHTI reported by Oberheide (2022) at 105 km and modeled by N. Pedatella (2022) in the MLT region. Thus, we conclude that these observed wind changes in the *F*-region are predominantly in response to SSW-modified tidal forcing. Figure 12 provides direct observational evidence that nighttime ionospheric depletions at *F*-region altitudes in the American sector are a robust feature of northern hemisphere SSWs, and also that they are forced through thermospheric wind modifications preeminently driven by SW2 amplification. Unfortunately, in normal science mode, the low inclination orbit of ICON prevents the MIGHTI instrument from viewing thermospheric winds at latitudes poleward of 10° S, which does not allow us to determine if meridional winds at higher southern latitudes were more poleward (southward) during this event. However, the increased poleward (northward) meridional winds in Figure 12g observed within the MIGHTI field-of-view, in conjunction with nudged TIME-GCM modeling results in Figures 4, 5 and 10 indicate that nighttime ionospheric depletions in the American sector are preferentially driven by increased poleward transport in response to SSWs.

4. Summary and Conclusions

Simulations and observations of nighttime ionospheric depletions in the *F*-region ionosphere during the January-February 2010, January 2013, and January 2021 SSWs were presented in this study. Through a combined data and modeling approach, we show that TIME-GCM simulations constrained by NAVGEM-HA reanalyses generally reproduce the nighttime ionospheric depletions in the American sector at *F*-region altitudes from GNSS and ionosonde observations originally reported by L. P. Goncharenko et al. (2018) for the January 2013 SSW, and shown herein for the January-February 2010 SSW. Nighttime ionospheric depletions in the American sector during these SSW events can be quite large, with N_mF_2 values reduced by 50% or more relative to their 27-day running mean values, and extend over ±50° in latitude.

Further evaluation of our constrained TIME-GCM simulations revealed that deep nighttime ionospheric depletions in the American sector coincided with days where SW2 (and other tidal components) amplitudes were enhanced (by a factor of 2–4) in the mesosphere and thermosphere due to altered SSW dynamics and forcing in the middle atmosphere. This resulted in strong tidally driven (mainly by SW2) neutral horizontal wind changes in the *F*-region ionosphere due to the SSW, concurrent with deep nighttime electron density depletions. Most notably there were important changes in *F*-region horizontal neutral winds, including significant enhancements in the westward winds (between 50 and 100 m s^{-1}), as well as large changes in the meridional winds that shifted to be more poleward (divergent) on either side of the magnetic equator during the January-February 2010 and January 2013 SSWs.

Mechanisms driving the changes in *F*-region electron density during the January 2013 SSW were then investigated. Following the hypothesis of G18, we individually investigated the SSW-altered *F*-region zonal and meridional wind contributions to the magnetic field aligned plasma motion in the O^+ continuity equation. Setting the neutral zonal wind contribution to zero in the O^+ continuity equation had little to no effect on the nighttime ionosphere in our TIME-GCM simulation. However, when the neutral meridional wind contribution to the magnetic field aligned ion (and hence electron) motion was significantly reduced, we found that deep nighttime electron density depletions were significantly reduced and approached baseline values from the TIME-GCM. This is particularly noteworthy considering SSW-driven neutral zonal wind changes were roughly a factor of 2 (or more) greater than SSW-driven neutral meridional wind changes at *F*-region altitudes. Based on force term analysis from the ion continuity equation for the January 2013 SSW, and similar coincident *F*-region electron density depletions and dynamical changes during the January-February 2010 SSW, a sequence of processes emerged to explain the presence of these deep nighttime ionospheric depletions in the American sector during SSW events: (a) Enhanced tidal forcing in response to a SSW acts to modify thermospheric meridional winds; (b) SSW-modified meridional winds at *F*-region altitudes reduce nighttime ionospheric electron densities via field-aligned plasma motion that induces downward ion and electron motion; (c) Downward motion transports plasma into a higher neutral density environment (i.e., more N_2 and O_2), leading to shorter chemical lifetimes, more loss, and ultimately a deep nighttime ionospheric depletion. Further, for the more recent January 2021 SSW, MERRA2 reanalyses, COSMIC-2/GIS electron density, and MIGHTI horizontal wind measurements revealed a deep nighttime *F*-region depletion in the American sector, indicating that such ionospheric depletions in the American sector are a robust feature during SSWs, and are a result of tidal modification of thermospheric winds.

Historically, upper atmospheric general circulation models have struggled to reproduce certain features in the nighttime ionosphere (e.g., Maute et al., 2012; Tsagouri et al., 2018). However, our results indicate that constraining an upper atmospheric general circulation model with reanalysis data throughout the entire middle atmosphere during a SSW provides a means to study the physical processes responsible for altering the nighttime ionosphere. We therefore suggest that additional modeling on ionospheric variations for other SSWs and longitude sectors at night using constrained upper atmospheric general circulation models would further our understanding of the interplay between dynamical and chemical processes in driving SSW-induced longitudinal variability in the nighttime ionosphere.

Acronyms

AIM	Aeronomy of Ice in the Mesosphere
CEDAR	Coupling, Energetics and Dynamics of Atmospheric Regions Program
COSMIC-2	Constellation Observing System for Meteorology, Ionosphere, and Climate 2
CTMT	Climatological Tidal Model of the Thermosphere
DMSP	Defense Meteorological Satellite Program
EUV	Extreme ultraviolet
EUVAC	EUV flux model for aeronomic calculations
F10.7	10.7 cm solar radio flux
FUV	Far ultraviolet
GIS	Global Ionospheric Specification
GNSS	Global Navigation Satellite System
GSWM	Global Scale Wave Model
HRDI	High-Resolution Doppler Imager
ICON	Ionospheric Connection Explorer
IVM	Ion velocity meter
MERRA2	Modern-Era Retrospective analysis for Research and Applications version 2
MIGHTI	Michelson Interferometer for Global High-Resolution Thermospheric Imaging
MLS	Microwave Limb Sounder
MLT	Mesosphere and lower thermosphere
NASA	National Aeronautics and Space Administration
NAVGEM-HA	Navy global environmental model a high-altitude version
NCAR	National Center for Atmospheric Research
RO	Radio occultation

SABER	Sounding of the atmosphere using broadband emission radiometry
SAMI3	Sami3 is Another Model of the Ionosphere
SD	Specified dynamics
SOFIE	Solar Occultation for Ice Experiment
SSMIS	Special Sensor Microwave Imager/Sounder
SSW	Sudden stratospheric warming
SW2	Semidiurnal migrating tide with zonal wave number 2
TEC	Total electron content
TGCM	Thermospheric general circulation model
TI	Thermosphere-ionosphere
TIDI	TIMED Doppler Interferometer
TIE-GCM	Thermosphere-ionosphere-electrodynamics general circulation model
TIME-GCM	Thermosphere-ionosphere-mesosphere-electrodynamics general circulation model
TIMED	Thermosphere ionosphere mesosphere energetics and dynamics
WACCM-X	Whole Atmosphere Community Climate Model with thermosphere-ionosphere eXtension
WINDII	Wind Imaging Interferometer

Data Availability Statement

The TIME-GCM code is made available by contacting the National Center for Atmospheric Research. The TIE-GCM code is available for download at https://www.hao.ucar.edu/modeling/tgcm/. The model output produced herein is reproducible from the TGCM model source code following the discussions and implementations of the nudging schemes and lower boundary conditions described thoroughly in Sections 2.4 and in Jones Jr. et al. (2018) and Jones Jr. et al. (2020). Daily NCAR TGCMs outputs in netCDF format from this study are archived on the DoD HPCMP long-term storage system. NAVGEM-HA inputs used to constrain the stratosphere and mesosphere of the TIME-GCM simulations performed herein are accessible at https://map.nrl.navy.mil (cd to map/pub/nrl/jgrspace2020/lightspecies/navgem/djfm1213 or map/pub/nrl/james2018/). GNSS-TEC data are publicly available through the CEDAR Madrigal database at http://cedar.openmadrigal.org. COSMIC-2 GIS data are publicly available after free registration at http://formosat7.earth.ncku.edu.tw/. ICON MIGHTI v04 winds were obtained from https://icon.ssl.berkeley.edu/Data/Data-Product-Matrix. MERRA-2 stratospheric zonal mean zonal winds and temperatures from NASA/GSFC Atmospheric Chemistry and Dynamics Laboratory at https://acd-ext.gsfc.nasa.gov/Data_services/met/ann_data.html website.

Acknowledgments
This work was supported by the NASA Early Career Investigator (NNH18ZDA001N-ECIP/18-ECIP_2–0018) and GOLD-ICON Guest Investigators (NNH20ZDA001N-GIGI/20-GIGI20_2–0009) Programs. KAZ was supported by the Office of Naval Research. LPG was also supported by the NASA Grant 80NSSC19K0262 and NASA GOLD-ICON Guest Investigators Grant 80NSSC22K0017. FG acknowledges support from NASA GOLD-ICON Guest Investigator Grant 80NSSC22K0019. These results are partly based upon work supported by the National Center for Atmospheric Research, which is a major facility sponsored by the National Science Foundation under Cooperative Agreement No. 1852977. NP acknowledges support from NASA Grants 80NSSC18K1046 and 80NSSC20K0628. Research, operations, and initial GNSS analysis at MIT Haystack Observatory are supported by the cooperative agreement AGS-1952737 between the US National Science Foundation and the Massachusetts Institute of Technology. The authors are grateful to Astrid Maute for a thoughtful review of this manuscript prior to submission. Computational resources for this work were provided by the U.S. Department of Defense (DoD) High Performance Computing Modernization Program (HPCMP).

References

Angelats i Coll, M., & Forbes, J. M. (2002). Nonlinear interactions in the upper atmosphere: The s = 1 and s = 3 nonmigrating semidiurnal tides. *Journal of Geophysical Research*, *107*(A8), SIA3-1–SIA3-15. https://doi.org/10.1029/2001JA900179

Bailey, S. M., Thurairajah, B., Randall, C. E., Holt, L., Siskind, D. E., Harvey, V. L., et al. (2014). A multi tracer analysis of thermosphere to stratosphere descent triggered by the 2013 stratospheric sudden warming. *Geophysical Research Letters*, *41*(14), 5216–5222. https://doi.org/10.1002/2014GL059860

Baldwin, M. P., Ayarzagüena, B., Birner, T., Butchart, N., Butler, A. H., Charlton-Perez, A. J., et al. (2021). Sudden stratospheric warmings. *Reviews of Geophysics*, *59*(1), e2020RG000708. https://doi.org/10.1029/2020RG000708

Bilitza, D., Altadill, D., Truhlik, V., Shubin, V., Galkin, I., Reinisch, B., & Huang, X. (2017). International reference ionosphere 2016: From ionospheric climate to real-time weather predictions. *Space Weather*, *15*(2), 418–429. https://doi.org/10.1002/2016sw001593

Butler, A. H., Seidel, D. J., Hardiman, S. C., Butchart, N., Birner, T., & Match, A. (2015). Defining sudden stratospheric warmings. *Bulletin of the American Meteorological Society*, *96*(11), 1913–1928. https://doi.org/10.1175/BAMS-D-13-00173.1

Cai, X., Burns, A. G., Wang, W., Qian, L., Pedatella, N., Coster, A., et al. (2021). Variations in thermosphere composition and ionosphere total electron content under geomagnetically quiet conditions at solar-minimum. *Geophysical Research Letters*, *48*(11), e2021GL093300. https://doi.org/10.1029/2021GL093300

Chau, J. L., Fejer, B. G., & Goncharenko, L. P. (2009). Quiet variability of equatorial e × b drifts during a sudden stratospheric warming event. *Geophysical Research Letters*, *36*(5), L05101. https://doi.org/10.1029/2008GL036785

Chau, J. L., Goncharenko, L. P., Fejer, B. G., & Liu, H.-L. (2012). Equatorial and low latitude ionospheric effects during sudden stratospheric warming events. *Space Science Reviews*, *168*(1), 385–417. https://doi.org/10.1007/s11214-011-9797-5

Dhadly, M. S., Emmert, J. T., Drob, D. P., McCormack, J. P., & Niciejewski, R. J. (2018). Short-term and interannual variations of migrating diurnal and semidiurnal tides in the mesosphere and lower thermosphere. *Journal of Geophysical Research: Space Physics*, *123*(8), 7106–7123. https://doi.org/10.1029/2018JA025748

Dickinson, R. E., Ridley, E. C., & Roble, R. G. (1984). Thermospheric general circulation with coupled dynamics and composition. *Journal of the Atmospheric Sciences*, *41*(2), 205–219. https://doi.org/10.1175/1520-0469(1984)041⟨0205:TGCWCD⟩2.0.CO;2

Eckermann, S. D., Ma, J., Hoppel, K. W., Kuhl, D. D., Allen, D. R., Doyle, J. A., et al. (2018). High-altitude (0-100 km) global atmospheric reanalysis system: Description and application to the 2014 Austral winter of the deep propagating gravity wave experiment (DEEPWAVE). *Monthly Weather Review*, *146*(8), 2639–2666. https://doi.org/10.1175/MWR-D-17-0386.1

Emery, B., Roble, R. G., Ridley, E., Richmond, A., Knipp, D., Crowley, G., et al. (2012). *Parameterization of the ion convection and the auroral oval in the NCAR thermospheric general circulation models (Technical Report)*. National Center for Atmospheric Research. https://doi.org/10.5065/D6N29TXZ

Englert, C. R., Harlander, J. M., Brown, C. M., & Marr, K. D. (2015). Spatial heterodyne spectroscopy at the naval research laboratory. *Applied Optics*, *54*(31), F158–F163. https://doi.org/10.1364/AO.54.00F158

Englert, C. R., Harlander, J. M., Brown, C. M., Marr, K. D., Miller, I. J., Stump, J. E., et al. (2017). Michelson interferometer for global high-resolution thermospheric imaging (mighti): Instrument design and calibration. *Space Science Reviews*, *212*(1), 553–584. https://doi.org/10.1007/s11214-017-0358-4

Fagundes, P. R., Goncharenko, L. P., de Abreu, A. J., Venkatesh, K., Pezzopane, M., de Jesus, R., et al. (2015). Ionospheric response to the 2009 sudden stratospheric warming over the equatorial, low, and middle latitudes in the south American sector. *Journal of Geophysical Research: Space Physics*, *120*(9), 7889–7902. https://doi.org/10.1002/2014JA020649

Fang, T.-W., Fuller-Rowell, T., Akmaev, R., Wu, F., Wang, H., & Anderson, D. (2012). Longitudinal variation of ionospheric vertical drifts during the 2009 sudden stratospheric warming. *Journal of Geophysical Research*, *117*(A3). https://doi.org/10.1029/2011JA017348

Fashae, J. B., Bolaji, O. S., & Rabiu, A. B. (2022). Response of the ionospheric tec to ssw and associated geomagnetic storm over the American low latitudinal sector. *Space Weather*, *20*(5), e2021SW002999. https://doi.org/10.1029/2021SW002999

Forbes, J. M. (1982). Atmospheric tide: 2. The solar and lunar semidiurnal components. *Journal of Geophysical Research*, *87*(A7), 5241–5252. https://doi.org/10.1029/JA087iA07p05241

Forbes, J. M., Oberheide, J., Zhang, X., Cullens, C., Englert, C. R., Harding, B. J., et al. (2022). Vertical coupling by solar semidiurnal tides in the thermosphere from icon/mighti measurements. *Journal of Geophysical Research: Space Physics*, *127*(5), e2022JA030288. https://doi.org/10.1029/2022JA030288

Forbes, J. M., Zhang, X., Ward, W., & Talaat, E. R. (2002). Climatological features of mesosphere and lower thermosphere stationary planetary waves within ±40° latitude. *Journal of Geophysical Research*, *107*(D17), ACL1-1–ACL1-14. https://doi.org/10.1029/2001JD001232

Gasperini, F., Crowley, G., Immel, T. J., & Harding, B. J. (2022). Vertical wave coupling in the low-latitude ionosphere-thermosphere as revealed by concurrent icon and cosmic-2 observations. *Space Science Reviews*, *218*(7), 55. https://doi.org/10.1007/s11214-022-00923-1

Gelaro, R., McCarty, W., Suárez, M. J., Todling, R., Molod, A., Takacs, L., et al. (2017). The modern-era retrospective analysis for research and applications, version 2 (merra-2). *Journal of Climate*, *30*(14), 5419–5454. https://doi.org/10.1175/JCLI-D-16-0758.1

Goncharenko, L., Chau, J. L., Condor, P., Coster, A., & Benkevitch, L. (2013). Ionospheric effects of sudden stratospheric warming during moderate-to-high solar activity: Case study of January 2013. *Geophysical Research Letters*, *40*(19), 4982–4986. https://doi.org/10.1002/grl.50980

Goncharenko, L., & Zhang, S.-R. (2008). Ionospheric signatures of sudden stratospheric warming: Ion temperature at middle latitude. *Geophysical Research Letters*, *35*(21), L21103. https://doi.org/10.1029/2008GL035684

Goncharenko, L. P., Chau, J. L., Liu, H.-L., & Coster, A. J. (2010). Unexpected connections between the stratosphere and ionosphere. *Geophysical Research Letters*, *37*(10). https://doi.org/10.1029/2010GL043125

Goncharenko, L. P., Coster, A. J., Chau, J. L., & Valladares, C. E. (2010). Impact of sudden stratospheric warmings on equatorial ionization anomaly. *Journal of Geophysical Research*, *115*(A10). https://doi.org/10.1029/2010JA015400

Goncharenko, L. P., Coster, A. J., Plumb, R. A., & Domeisen, D. I. V. (2012). The potential role of stratospheric ozone in the stratosphere-ionosphere coupling during stratospheric warmings. *Geophysical Research Letters*, *39*(8). https://doi.org/10.1029/2012GL051261

Goncharenko, L. P., Coster, A. J., Zhang, S.-R., Erickson, P. J., Benkevitch, L., Aponte, N., et al. (2018). Deep ionospheric hole created by sudden stratospheric warming in the nighttime ionosphere. *Journal of Geophysical Research: Space Physics*, *123*(9), 7621–7633. https://doi.org/10.1029/2018JA025541

Goncharenko, L. P., Harvey, V. L., Liu, H., & Pedatella, N. M. (2021). Sudden stratospheric warming impacts on the ionosphere-thermosphere system. In *Ionosphere dynamics and applications* (pp. 369–400). American Geophysical Union (AGU). https://doi.org/10.1002/9781119815617.ch16

Goncharenko, L. P., Hsu, V. W., Brum, C. G. M., Zhang, S.-R., & Fentzke, J. T. (2013). Wave signatures in the midlatitude ionosphere during a sudden stratospheric warming of January 2010. *Journal of Geophysical Research: Space Physics*, *118*(1), 472–487. https://doi.org/10.1029/2012JA018251

Heelis, R. A., Lowell, J. K., & Spiro, R. W. (1982). A model of the high-latitude ionospheric convection pattern. *Journal of Geophysical Research*, *87*(A8), 6339–6345. https://doi.org/10.1029/JA087iA08p06339

Hogan, T. F., Liu, M., Ridout, J. A., Peng, M. S., Whitcomb, T. R., Ruston, B. C., et al. (2014). The navy global environmental model. *Oceanography*, *27*(3), 116–125. https://doi.org/10.5670/oceanog.2014.73

Huba, J. D., Joyce, G., & Fedder, J. A. (2000). Sami2 is another model of the ionosphere (sami2): A new low-latitude ionosphere model. *Journal of Geophysical Research*, *105*(A10), 23035–23053. https://doi.org/10.1029/2000JA000035

Huba, J. D., Joyce, G., & Krall, J. (2008). Three-dimensional equatorial spread f modeling. *Geophysical Research Letters*, *35*(10). https://doi.org/10.1029/2008GL033509

Immel, T. J., England, S. L., Mende, S. B., Heelis, R. A., Englert, C. R., Edelstein, J., et al. (2017). The ionospheric connection explorer mission: Mission goals and design. *Space Science Reviews*, *214*(1), 13. https://doi.org/10.1007/s11214-017-0449-2

Jin, H., Miyoshi, Y., Pancheva, D., Mukhtarov, P., Fujiwara, H., & Shinagawa, H. (2012). Response of migrating tides to the stratospheric sudden warming in 2009 and their effects on the ionosphere studied by a whole atmosphere-ionosphere model GAIA with COSMIC and TIMED/SABER observations. *Journal of Geophysical Research*, *117*(A10). https://doi.org/10.1029/2012JA017650

Jonah, O. F., de Paula, E. R., Kherani, E. A., Dutra, S. L. G., & Paes, R. R. (2014). Atmospheric and ionospheric response to sudden stratospheric warming of January 2013. *Journal of Geophysical Research: Space Physics*, *119*(6), 4973–4980. https://doi.org/10.1002/2013JA019491

Jones, M., Forbes, J. M., Hagan, M. E., & Maute, A. (2014). Impacts of vertically propagating tides on the mean state of the ionosphere-thermosphere system. *Journal of Geophysical Research: Space Physics*, *119*(3), 2197–2213. https://doi.org/10.1002/2013JA019744

Jones, M., Jr., Drob, D. P., Siskind, D. E., McCormack, J. P., Maute, A., McDonald, S. E., & Dymond, K. F. (2018). Evaluating different techniques for constraining lower atmospheric variability in an upper atmosphere general circulation model: A case study during the 2010 sudden stratospheric warming. *Journal of Advances in Modeling Earth Systems*, *10*(12), 3076–3102. https://doi.org/10.1029/2018MS001440

Jones, M., Jr., Forbes, J. M., Hagan, M. E., & Maute, A. (2013). Non-migrating tides in the ionosphere-thermosphere: In situ versus tropospheric sources. *Journal of Geophysical Research: Space Physics*, *118*(5), 2438–2451. https://doi.org/10.1002/jgra.50257

Jones, M., Jr., Forbes, J. M., & Sassi, F. (2019). The effects of vertically propagating tides on the mean dynamical structure of the lower thermosphere. *Journal of Geophysical Research: Space Physics*, *124*(8), 7202–7219. https://doi.org/10.1029/2019JA026934

Jones, M., Jr., Siskind, D. E., Drob, D. P., McCormack, J. P., Emmert, J. T., Dhadly, M. S., et al. (2020). Coupling from the middle atmosphere to the exobase: Dynamical disturbance effects on light chemical species. *Journal of Geophysical Research: Space Physics*, *125*(10), e2020JA028331. https://doi.org/10.1029/2020JA028331

Killeen, T. L., Skinner, W. R., Johnson, R. M., Edmonson, C. J., Wu, Q., Niciejewski, R. J., et al. (1999). TIMED Doppler interferometer (TIDI). In A. M. Larar (Ed.), *Optical spectroscopic techniques and instrumentation for atmospheric and space research III* (Vol. 3756, pp. 289–301). SPIE. https://doi.org/10.1117/12.366383

Killeen, T. L., Wu, Q., Solomon, S. C., Ortland, D. A., Skinner, W. R., Niciejewski, R. J., & Gell, D. A. (2006). Timed Doppler interferometer: Overview and recent results. *Journal of Geophysical Research*, *111*(A10), A10S01. https://doi.org/10.1029/2005JA011484

Lei, J., Wang, W., Burns, A. G., Solomon, S. C., Richmond, A. D., Wiltberger, M., et al. (2008). Observations and simulations of the ionospheric and thermospheric response to the December 2006 geomagnetic storm: Initial phase. *Journal of Geophysical Research*, *113*(A1). https://doi.org/10.1029/2007JA012807

Lieberman, R. S., Harding, B. J., Heelis, R. A., Pedatella, N. M., Forbes, J. M., & Oberheide, J. (2022). Atmospheric lunar tide in the low latitude thermosphere-ionosphere. *Geophysical Research Letters*, *49*(11), e2022GL098078. https://doi.org/10.1029/2022GL098078

Limpasuvan, V., Orsolini, Y. J., Chandran, A., Garcia, R. R., & Smith, A. K. (2016). On the composite response of the mlt to major sudden stratospheric warming events with elevated stratopause. *Journal of Geophysical Research: Atmospheres*, *121*(9), 4518–4537. https://doi.org/10.1002/2015JD024401

Lin, C.-Y., Lin, C. C.-H., Liu, J.-Y., Rajesh, P. K., Matsuo, T., Chou, M.-Y., et al. (2020). The early results and validation of formosat-7/cosmic-2 space weather products: Global ionospheric specification and ne-aided abel electron density profile. *Journal of Geophysical Research: Space Physics*, *125*(10), e2020JA028028. https://doi.org/10.1029/2020JA028028

Lin, C. Y., Matsuo, T., Liu, J. Y., Lin, C. H., Huba, J. D., Tsai, H. F., & Chen, C. Y. (2017). Data assimilation of ground-based gps and radio occultation total electron content for global ionospheric specification. *Journal of Geophysical Research: Space Physics*, *122*(10), 10876–10886. https://doi.org/10.1002/2017JA024185

Lin, C. Y., Matsuo, T., Liu, J. Y., Lin, C. H., Tsai, H. F., & Araujo-Pradere, E. A. (2015). Ionospheric assimilation of radio occultation and ground-based GPS data using non-stationary background model error covariance. *Atmospheric Measurement Techniques*, *8*(1), 171–182. https://doi.org/10.5194/amt-8-171-2015

Lin, J. T., Lin, C. H., Rajesh, P. K., Yue, J., Lin, C. Y., & Matsuo, T. (2020). Local-time and vertical characteristics of quasi-6-day oscillation in the ionosphere during the 2019 Antarctic sudden stratospheric warming. *Geophysical Research Letters*, *47*(21), e2020GL090345. https://doi.org/10.1029/2020GL090345

Lindzen, R. S., Hong, S. S., & Forbes, J. M. (1977). *Semidiurnal hough mode extensions in the thermosphere and their application (Memorandum Report No. 3442)*. Naval Research Laboratory.

Liu, G., Janches, D., Ma, J., Lieberman, R. S., Stober, G., Moffat-Griffin, T., et al. (2022). Mesosphere and lower thermosphere winds and tidal variations during the 2019 Antarctic sudden stratospheric warming. *Journal of Geophysical Research: Space Physics*, *127*(3), e2021JA030177. https://doi.org/10.1029/2021JA030177

Liu, H. L. (2016). Variability and predictability of the space environment as related to lower atmosphere forcing. *Space Weather*, *14*(9), 634–658. https://doi.org/10.1002/2016SW001450

Liu, J., Wang, W., Burns, A., Solomon, S. C., Zhang, S., Zhang, Y., & Huang, C. (2016). Relative importance of horizontal and vertical transports to the formation of ionospheric storm-enhanced density and polar tongue of ionization. *Journal of Geophysical Research: Space Physics*, *121*(8), 8121–8133. https://doi.org/10.1002/2016JA022882

Lu, G., Zakharenkova, I., Cherniak, I., & Dang, T. (2020). Large-scale ionospheric disturbances during the 17 March 2015 storm: A model-data comparative study. *Journal of Geophysical Research: Space Physics*, *125*(5), e2019JA027726. https://doi.org/10.1029/2019JA027726

Lu, Q., Rao, J., Liang, Z., Guo, D., Luo, J., Liu, S., et al. (2021). The sudden stratospheric warming in January 2021. *Environmental Research Letters*, *16*(8), 084029. https://doi.org/10.1088/1748-9326/ac12f4

Makela, J. J., Baughman, M., Navarro, L. A., Harding, B. J., Englert, C. R., Harlander, J. M., et al. (2021). Validation of icon-mighti thermospheric wind observations: 1. Nighttime red-line ground-based fabry-perot interferometers. *Journal of Geophysical Research: Space Physics*, *126*(2), e2020JA028726. https://doi.org/10.1029/2020JA028726

Manney, G. L., Schwartz, M. J., Krüger, K., Santee, M. L., Pawson, S., Lee, J. N., et al. (2009). Aura microwave limb sounder observations of dynamics and transport during the record-breaking 2009 arctic stratospheric major warming. *Geophysical Research Letters*, *36*(12), L12815. https://doi.org/10.1029/2009GL038586

Maute, A., Hagan, M. E., Yudin, V., Liu, H.-L., & Yizengaw, E. (2015). Causes of the longitudinal differences in the equatorial vertical E × B drift during the 2013 SSW period as simulated by the TIME-GCM. *Journal of Geophysical Research: Space Physics*, *120*(6), 5117–5136. https://doi.org/10.1002/2015JA021126

Maute, A., Richmond, A. D., & Roble, R. G. (2012). Sources of low-latitude ionospheric e × b drifts and their variability. *Journal of Geophysical Research*, *117*(A6). https://doi.org/10.1029/2011JA017502

McCarty, W., Coy, L., Gelaro, R., Huang, A., Merkova, D., Smith, E. B., et al. (2016). *Merra-2 input observations: Summary and assessment, NASA technical report series on global modeling and data assimilation (Tech. Rep. Nos. NASA/TM-2016-104606, 46)*. NASA Goddard Space Flight Center.

McCormack, J., Hoppel, K., Kuhl, D., de Wit, R., Stober, G., Espy, P., et al. (2017). Comparison of mesospheric winds from a high-altitude meteorological analysis system and meteor radar observations during the boreal winters of 2009-2010 and 2012-2013. *Journal of Atmospheric and Solar-Terrestrial Physics*, *154*, 132–166. https://doi.org/10.1016/j.jastp.2016.12.007

McDonald, S., Sassi, F., Tate, J., McCormack, J., Kuhl, D., Drob, D., et al. (2018). Impact of non-migrating tides on the low latitude ionosphere during a sudden stratospheric warming event in january 2010. *Journal of Atmospheric and Solar-Terrestrial Physics*, *171*, 188–200. https://doi.org/10.1016/j.jastp.2017.09.012

Miyoshi, Y., Fujiwara, H., Jin, H., & Shinagawa, H. (2015). Impacts of sudden stratospheric warming on general circulation of the thermosphere. *Journal of Geophysical Research: Space Physics*, *120*(12), 10897–10912. https://doi.org/10.1002/2015JA021894

Mošna, Z., Edemskiy, I., Laštovička, J., Kozubek, M., Knížová Koucká, P., Kouba, D., & Siddiqui, T. A. (2021). Observation of the ionosphere in middle latitudes during 2009, 2018 and 2018/2019 sudden stratospheric warming events. *Atmosphere*, *12*(5), 602. https://doi.org/10.3390/atmos12050602

Niciejewski, R., Wu, Q., Skinner, W., Gell, D., Cooper, M., Marshall, A., et al. (2006). TIMED Doppler interferometer on the thermosphere ionosphere mesosphere energetics and dynamics satellite: Data product overview. *Journal of Geophysical Research*, *111*(A11), A11S90. https://doi.org/10.1029/2005JA011513

Oberheide, J. (2022). Day-to-day variability of the semidiurnal tide in the f-region ionosphere during the January 2021 SSW from cosmic-2 and icon. *Geophysical Research Letters*, *49*(17), e2022GL100369. https://doi.org/10.1029/2022GL100369

Oberheide, J., Forbes, J. M., Zhang, X., & Bruinsma, S. L. (2011). Climatology of upward propagating diurnal and semidiurnal tides in the thermosphere. *Journal of Geophysical Research*, *116*(A11). https://doi.org/10.1029/2011JA016784

Oberheide, J., Pedatella, N. M., Gan, Q., Kumari, K., Burns, A. G., & Eastes, R. W. (2020). Thermospheric composition o/n response to an altered meridional mean circulation during sudden stratospheric warmings observed by gold. *Geophysical Research Letters*, *47*(1), e2019GL086313. https://doi.org/10.1029/2019GL086313

Paes, R. R., Batista, I. S., Candido, C. M. N., Jonah, O. F., & Santos, P. C. P. (2014). Equatorial ionization anomaly variability over the Brazilian region during boreal sudden stratospheric warming events. *Journal of Geophysical Research: Space Physics*, *119*(9), 7649–7664. https://doi.org/10.1002/2014JA019968

Pancheva, D., Mukhtarov, P., & Andonov, B. (2009). Nonmigrating tidal activity related to the sudden stratospheric warming in the arctic winter of 2003/2004. *Annales Geophysicae*, *27*(3), 975–987. https://doi.org/10.5194/angeo-27-975-2009

Pedatella, N. (2022). Ionospheric variability during the 2020-2021 SSW: Cosmic-2 observations and waccm-x simulations. *Atmosphere*, *13*(3), 368. https://doi.org/10.3390/atmos13030368

Pedatella, N. M. (2016). Impact of the lower atmosphere on the ionosphere response to a geomagnetic superstorm. *Geophysical Research Letters*, *43*(18), 9383–9389. https://doi.org/10.1002/2016GL070592

Pedatella, N. M., Chau, J. L., Schmidt, H., Goncharenko, L. P., Stolle, C., Hocke, K., et al. (2018). How sudden stratospheric warming affects the whole atmosphere. *Eos*, *99*. https://doi.org/10.1029/2018EO092441

Pedatella, N. M., & Liu, H. L. (2013). The influence of atmospheric tide and planetary wave variability during sudden stratosphere warmings on the low latitude ionosphere. *Journal of Geophysical Research: Space Physics*, *118*(8), 5333–5347. https://doi.org/10.1002/jgra.50492

Pedatella, N. M., Liu, H.-L., & Richmond, A. D. (2012). Atmospheric semidiurnal lunar tide climatology simulated by the whole atmosphere community climate model. *Journal of Geophysical Research*, *117*(A6). https://doi.org/10.1029/2012JA017792

Pedatella, N. M., Liu, H.-L., Sassi, F., Lei, J., Chau, J. L., & Zhang, X. (2014). Ionosphere variability during the 2009 ssw: Influence of the lunar semidiurnal tide and mechanisms producing electron density variability. *Journal of Geophysical Research: Space Physics*, *119*(5), 3828–3843. https://doi.org/10.1002/2014JA019849

Pedatella, N. M., & Maute, A. (2015). Impact of the semidiurnal lunar tide on the midlatitude thermospheric wind and ionosphere during sudden stratosphere warmings. *Journal of Geophysical Research: Space Physics*, *120*(12), 10740–10753. https://doi.org/10.1002/2015JA021986

Pedatella, N. M., Richmond, A. D., Maute, A., & Liu, H.-L. (2016). Impact of semidiurnal tidal variability during SSWs on the mean state of the ionosphere and thermosphere. *Journal of Geophysical Research: Space Physics*, *121*(8), 8077–8088. https://doi.org/10.1002/2016JA022910

Qian, L., Burns, A. G., Emery, B. A., Foster, B., Lu, G., Maute, A., et al. (2014). The NCAR TIE-GCM. In *Modeling the ionosphere-thermosphere system* (pp. 73–83). American Geophysical Union (AGU). https://doi.org/10.1002/9781118704417.ch7

Rajesh, P. K., Lin, C. C., Lin, J.-T., Lin, C.-Y., Yue, J., Matsuo, T., et al. (2021). Day-to-day variability of ionosphere electron density during solar minimum derived from formosat-7/cosmic-2 measurements. *Terrestrial, Atmospheric and Oceanic Sciences*, *32*(6.1). https://doi.org/10.3319/tao.2021.08.01.01

Rao, J., Garfinkel, C. I., Wu, T., Lu, Y., Lu, Q., & Liang, Z. (2021). The January 2021 sudden stratospheric warming and its prediction in subseasonal to seasonal models. *Journal of Geophysical Research: Atmospheres*, *126*(21), e2021JD035057. https://doi.org/10.1029/2021JD035057

Rezac, L., Kutepov, A., Russell, J., Feofilov, A., Yue, J., & Goldberg, R. (2015). Simultaneous retrieval of $t(p)$ and co_2 VMR from two-channel non-LTE limb radiances and application to daytime SABER/TIMED measurements. *Journal of Atmospheric and Solar-Terrestrial Physics*, *130–131*, 23–42. https://doi.org/10.1016/j.jastp.2015.05.004

Ribeiro, B., Fagundes, P., Venkatesh, K., Tardelli, A., Pillat, V., & Seemala, G. (2019). Equatorial and low-latitude positive ionospheric phases due to moderate geomagnetic storm during high solar activity in January 2013. *Advances in Space Research*, *64*(4), 995–1010. https://doi.org/10.1016/j.asr.2019.05.032

Richards, P. G., Fennelly, J. A., & Torr, D. G. (1994). EUVAC: A solar Euv flux model for aeronomic calculations. *Journal of Geophysical Research*, *99*(A5), 8981–8992. https://doi.org/10.1029/94JA00518

Richmond, A. D., Ridley, E. C., & Roble, R. G. (1992). A thermosphere/ionosphere general circulation model with coupled electrodynamics. *Geophysical Research Letters*, *19*(6), 601–604. https://doi.org/10.1029/92GL00401

Rideout, W., & Coster, A. (2006). Automated GPS processing for global total electron content data. *GPS Solutions*, *10*(3), 219–228. https://doi.org/10.1007/s10291-006-0029-5

Rienecker, M. M., Suarez, M. J., Gelaro, R., Todling, R., Bacmeister, J., Liu, E., et al. (2011). Merra: Nasa's modern-era retrospective analysis for research and applications. *Journal of Climate*, *24*(14), 3624–3648. https://doi.org/10.1175/JCLI-D-11-00015.1

Roble, R. G. (1996). The NCAR thermosphere-ionosphere-mesosphere-electrodynamics general circulation model (TIME-GCM). In *Step handbook on ionospheric models* (pp. 281–288). Utah State University.

Roble, R. G., & Ridley, E. (1987). An auroral model for the NCAR thermospheric general circulation model (TGCM). *Annales Geophysicae*, *5A*, 369–382. Retrieved from http://n2t.net/ark:/85065/d70v8ckz

Roble, R. G., & Ridley, E. C. (1994). A thermosphere-ionosphere-mesosphere-electrodynamics general circulation model (time-GCM): Equinox solar cycle minimum simulations (30-500 km). *Geophysical Research Letters*, *21*(6), 417–420. https://doi.org/10.1029/93GL03391

Roble, R. G., Ridley, E. C., Richmond, A. D., & Dickinson, R. E. (1988). A coupled thermosphere/ionosphere general circulation model. *Geophysical Research Letters*, *15*(12), 1325–1328. https://doi.org/10.1029/GL015i012p01325

Siddiqui, T. A., Maute, A., & Pedatella, N. M. (2019). On the importance of interactive ozone chemistry in earth-system models for studying mesophere-lower thermosphere tidal changes during sudden stratospheric warmings. *Journal of Geophysical Research: Space Physics*, *124*(12), 10690–10707. https://doi.org/10.1029/2019JA027193

Siddiqui, T. A., Yamazaki, Y., Stolle, C., Maute, A., Laštovička, J., Edemskiy, I. K., et al. (2021). Understanding the total electron content variability over Europe during 2009 and 2019 ssws. *Journal of Geophysical Research: Space Physics*, *126*(9), e2020JA028751. https://doi.org/10.1029/2020JA028751

Siskind, D. E., Drob, D. P., Dymond, K. F., & McCormack, J. P. (2014). Simulations of the effects of vertical transport on the thermosphere and ionosphere using two coupled models. *Journal of Geophysical Research: Space Physics*, *119*(2), 1172–1185. https://doi.org/10.1002/2013JA019116

Siskind, D. E., Eckermann, S. D., McCormack, J. P., Coy, L., Hoppel, K. W., & Baker, N. L. (2010). Case studies of the mesospheric response to recent minor, major, and extended stratospheric warmings. *Journal of Geophysical Research*, *115*(D3), D00N03. https://doi.org/10.1029/2010JD014114

Siskind, D. E., Harvey, V. L., Sassi, F., McCormack, J. P., Randall, C. E., Hervig, M. E., & Bailey, S. M. (2021). Two- and three-dimensional structures of the descent of mesospheric trace constituents after the 2013 sudden stratospheric warming elevated stratopause event. *Atmospheric Chemistry and Physics*, *21*(18), 14059–14077. https://doi.org/10.5194/acp-21-14059-2021

Siskind, D. E., Jones, M., Jr., Drob, D. P., McCormack, J. P., Hervig, M. E., Marsh, D. R., et al. (2019). On the relative roles of dynamics and chemistry governing the abundance and diurnal variation of low-latitude thermospheric nitric oxide. *Annales Geophysicae*, *37*(1), 37–48. https://doi.org/10.5194/angeo-37-37-2019

Smith, A. K., Pedatella, N. M., Marsh, D. R., & Matsuo, T. (2017). On the dynamical control of the mesosphere-lower thermosphere by the lower and middle atmosphere. *Journal of the Atmospheric Sciences*, *74*(3), 933–947. https://doi.org/10.1175/JAS-D-16-0226.1

Solomon, S. C., & Qian, L. (2005). Solar extreme-ultraviolet irradiance for general circulation models. *Journal of Geophysical Research*, *110*(A10), A10306. https://doi.org/10.1029/2005JA011160

Sridharan, S., Sathishkumar, S., & Gurubaran, S. (2012). Variabilities of mesospheric tides during sudden stratospheric warming events of 2006 and 2009 and their relationship with ozone and water vapour. *Journal of Atmospheric and Solar-Terrestrial Physics*, *78–79*, 108–115. https://doi.org/10.1016/j.jastp.2011.03.013

Stauffer, D. R., & Seaman, N. L. (1990). Use of four-dimensional data assimilation in a limited-area mesoscale model. Part I: Experiments with synoptic-scale data. *Monthly Weather Review*, *118*(6), 1250–1277. https://doi.org/10.1175/1520-0493(1990)118⟨1250:UOFDDA⟩2.0.CO;2

Stauffer, D. R., & Seaman, N. L. (1994). Multiscale four-dimensional data assimilation. *Journal of Applied Meteorology*, *33*(3), 416–434. https://doi.org/10.1175/1520-0450(1994)033⟨0416:MFDDA⟩2.0.CO;2

Stening, R. J. (1977). Electron density profile changes associated with the equatorial electrojet. *Journal of Atmospheric and Terrestrial Physics*, *39*(2), 157–164. https://doi.org/10.1016/0021-9169(77)90109-X

Stening, R. J., Meek, C. E., & Manson, A. H. (1996). Upper atmosphere wind systems during reverse equatorial electrojet events. *Geophysical Research Letters*, *23*(22), 3243–3246. https://doi.org/10.1029/96GL02611

Stober, G., Baumgarten, K., McCormack, J. P., Brown, P., & Czarnecki, J. (2020). Comparative study between ground-based observations and navgem-ha analysis data in the mesosphere and lower thermosphere region. *Atmospheric Chemistry and Physics*, *20*(20), 11979–12010. https://doi.org/10.5194/acp-20-11979-2020

Sumod, S., Pant, T., Jose, L., Hossain, M., & Kumar, K. (2012). Signatures of sudden stratospheric warming on the equatorial ionosphere-thermosphere system. *Planetary and Space Science*, *63–64*, 49–55. https://doi.org/10.1016/j.pss.2011.08.005

Swadley, S. D., Poe, G. A., Bell, W., Hong, Y., Kunkee, D. B., McDermid, I. S., & Leblanc, T. (2008). Analysis and characterization of the SSMIS upper atmosphere sounding channel measurements. *IEEE Transactions on Geoscience and Remote Sensing*, *46*(4), 962–983. https://doi.org/10.1109/TGRS.2008.916980

Tsagouri, I., Goncharenko, L., Shim, J. S., Belehaki, A., Buresova, D., & Kuznetsova, M. M. (2018). Assessment of current capabilities in modeling the ionospheric climatology for space weather applications: FoF2 and HMF2. *Space Weather*, *16*(12), 1930–1945. https://doi.org/10.1029/2018SW002035

Woods, T. N., & Rottman, G. J. (2002). Solar ultraviolet variability over time periods of aeronomic interest. In *Atmospheres in the solar system: Comparative aeronomy* (pp. 221–233). American Geophysical Union (AGU). https://doi.org/10.1029/130GM14

Wu, Q., & Nozawa, S. (2015). Mesospheric and thermospheric observations of the January 2010 stratospheric warming event. *Journal of Atmospheric and Solar-Terrestrial Physics*, *123*, 22–38. https://doi.org/10.1016/j.jastp.2014.11.006

Yamazaki, Y., Matthias, V., Miyoshi, Y., Stolle, C., Siddiqui, T., Kervalishvili, G., et al. (2020). September 2019 Antarctic sudden stratospheric warming: Quasi-6-day wave burst and ionospheric effects. *Geophysical Research Letters*, *47*(1), e2019GL086577. https://doi.org/10.1029/2019GL086577

Yan, X., Wright, J. S., Zheng, X., Livesey, N. J., Vömel, H., & Zhou, X. (2016). Validation of aura MLS retrievals of temperature, water vapour and ozone in the upper troposphere and lower–middle stratosphere over the Tibetan plateau during boreal summer. *Atmospheric Measurement Techniques*, *9*(8), 3547–3566. https://doi.org/10.5194/amt-9-3547-2016

Yiğit, E., & Medvedev, A. S. (2016). Role of gravity waves in vertical coupling during sudden stratospheric warmings. *Geoscience Letters*, *3*(1), 27. https://doi.org/10.1186/s40562-016-0056-1

Zhang, R., Liu, L., Ma, H., Chen, Y., & Le, H. (2022). Icon observations of equatorial ionospheric vertical exb and field-aligned plasma drifts during the 2020?2021 SSW. *Geophysical Research Letters*, *49*(16), e2022GL099238. https://doi.org/10.1029/2022GL099238

Zhang, S.-R., Foster, J. C., Holt, J. M., Erickson, P. J., & Coster, A. J. (2012). Magnetic declination and zonal wind effects on longitudinal differences of ionospheric electron density at midlatitudes. *Journal of Geophysical Research*, *117*(A8). https://doi.org/10.1029/2012JA017954

Zhang, X., Forbes, J. M., & Hagan, M. E. (2010a). Longitudinal variation of tides in the MLT region: 1. Tides driven by tropospheric net radiative heating. *Journal of Geophysical Research*, *115*(A6). https://doi.org/10.1029/2009JA014897

Zhang, X., Forbes, J. M., & Hagan, M. E. (2010b). Longitudinal variation of tides in the MLT region: 2. Relative effects of solar radiative and latent heating. *Journal of Geophysical Research*, *115*(A6). https://doi.org/10.1029/2009JA014898